A Sphingomyelin-Sensing Pathway Governing Metabolic Inflammation

Authors

Jianfei Zheng[1]†, Chunling Xu[2]†, Zhuo Wang[2]†, Tao Yao[3,4]†, Haodong Wang[1,5]†, Xubo Lin[6], Kangling Zhu[1,7], Yurong Liu[1], Dong Peng[2], Fengwu Chen[1], Zhewen Qin[3,4], Min Zhang[2]*, Bo Shan[3,4]*, and Liang Ge[1]*

Affiliation

[1]State Key Laboratory of Membrane Biology, Tsinghua-Peking Center for Life Sciences, Beijing Frontier Research Center for Biological Structure, School of Life Sciences, Tsinghua University, Beijing, 100084, China.

[2]School of Pharmaceutical Sciences, Tsinghua University, Beijing, 100084, China.

[3]Zhejiang Key Laboratory of Pancreatic Disease, The First Affiliated Hospital, Zhejiang Key Laboratory of Frontier Medical Research on Cancer Metabolism, and Institute of Translational Medicine, Zhejiang University School of Medicine, Hangzhou, Zhejiang, 310029, China.

[4]Institute of Fundamental and Transdisciplinary Research, Cancer Center, Zhejiang University, Hangzhou, Zhejiang, China.

[5]Department of Biochemistry and Biophysics, Weill Cornell Medical College,1300 York Ave, New York, NY 10065, USA

[6]Beijing Advanced Innovation Center for Biomedical Engineering, Beihang University, Beijing 100191, China

[7]Academy for Advanced Interdisciplinary Studies, Beijing, Peking University, 100871, China.

*Corresponding author. Email: zhangmin143@mail.tsinghua.edu.cn; boshan@zju.edu.cn; liangge@mail.tsinghua.edu.cn

†These authors contributed equally to this work.

Abstract

Obesity-associated metabolic inflammation is driven by lipid-laden macrophages that release proinflammatory cytokines such as interleukin-1β, yet how macrophages sense lipid overload to trigger inflammation remains unclear. Here, we identify sphingomyelin sensing as a key mechanism linking lipid metabolism to inflammatory activation. We show that macrophages detect specific sphingomyelin species to induce metabolic inflammation through the TMED10-channeled unconventional secretion (THU) pathway, a recently discovered non-lytic route for cytokine release distinct from GSDMD-dependent pyroptosis. Single-cell transcriptomic profiling revealed a metabolic inflammation macrophage subset with enhanced lipid uptake, active sphingomyelin metabolism, and elevated TMED10 expression, marking a population tuned to metabolic stress and inflammation. A high-fat diet feeding induced a shift toward medium-chain sphingomyelin species in the adipose tissue macrophages, which potently activated TMED10 and promoted IL-1β secretion via the THU pathway. TMED10 directly binds sphingomyelin through its transmembrane domain, with residue Q204 being essential for this interaction. TMED10 displays high sensitivity to medium-chain sphingomyelin (EC_{50} ≈ 0.5%), underscoring its role as a precise lipid sensor. Mutation of Q204 disrupted sphingomyelin

binding, impaired IL-1β release, and protected mice from metabolic inflammation. Together, these findings establish a TMED10-sphingomyelin axis as a molecular circuit that senses lipid composition to drive chronic inflammation, revealing new therapeutic opportunities for obesity and other lipid-associated inflammatory disorders.

Main

Obesity, affecting over one billion individuals worldwide, lies at the core of the global metabolic disease epidemic[1]. A major pathological consequence of obesity is chronic, low-grade inflammation—referred to as metabolic inflammation—driven by lipid-engorged macrophages within adipose tissue that secrete proinflammatory cytokines such as interleukin-1β (IL-1β)[2-7]. The persistent production of these cytokines leads to systemic metabolic dysfunction, including insulin resistance and dyslipidemia[8-10]. A substantial body of evidence links lipid metabolic rewiring to the functional remodeling of heterogeneous adipose tissue macrophages (ATMs) during obesity[11-18]; however, the mechanistic connections between lipid metabolism and macrophage activation—particularly their inflammatory responses leading to metabolic inflammation—remain poorly defined.

In contrast to the limited understanding of chronic inflammation in obesity, bacteria-induced acute inflammation is well characterized and is predominantly mediated by Gasdermin D (GSDMD)–dependent pore formation in macrophages, a process that typically culminates in pyroptotic cell death and drives the rapid release of proinflammatory cytokines such as IL-1β[19-22]. Notably, obesity-associated chronic inflammatory states and GSDMD-mediated acute inflammation share several upstream signaling modules, including Toll-like receptor engagement, inflammasome activation, and caspase-dependent processing[23-25]. The convergence of these pathways prompted us to investigate whether GSDMD also contributes to cytokine release in macrophages experiencing metabolic stress–induced chronic inflammation.

GSDMD is dispensable for high-fat diet–induced metabolic inflammation

To assess the role of macrophage GSDMD in metabolic inflammation, we generated *Lyz2*–cre *GSDMD*$^{fl/fl}$ mice, in which GSDMD is specifically deleted in myeloid lineage cells, including macrophages. Consistent with previous reports[19-21], GSDMD-deficient macrophages exhibited markedly reduced IL-1β release in response to LPS plus nigericin or ATP stimulation (Fig. 1a), recapitulating acute inflammatory conditions. In vivo, GSDMD myeloid cell lineage-specific knockout significantly decreased IL-1β levels in both plasma and peritoneal fluid following LPS challenge and prolonged the survival of LPS-treated mice (Fig. 1b,c), confirming the established role of GSDMD in acute inflammation[19,26,27].

We next examined whether GSDMD in macrophages contributes to obesity–induced chronic metabolic inflammation. Surprisingly, plasma IL-1β levels were comparable between control (*GSDMD*$^{fl/fl}$) and *Lyz2*–cre *GSDMD*$^{fl/fl}$ mice after long-term high-fat diet (HFD) feeding (Fig. 1d). Loss of macrophage GSDMD didn't alter adipocyte hypotrophy or crown-like structure (CLS) formation in epididymal white adipose tissue (eWAT) (Fig. 1e). In agreement, transcriptomic profiling revealed no significant changes in inflammatory gene expression in GSDMD-deficient

mice (Fig. 1f,g and Supplementary Table 1). Furthermore, systemic metabolic testing showed that *Lyz2*–cre *GSDMD*$^{fl/fl}$ and control mice displayed comparable glucose tolerance and insulin sensitivity under both normal chow diet (ND) and HFD feeding, as determined by glucose tolerance tests (GTT) and insulin tolerance tests (ITT) (Fig. 1h). Collectively, these findings indicate that GSDMD-mediated inflammatory cytokine release, which drives acute inflammation, is not required for HFD-induced metabolic inflammation, suggesting the involvement of alternative macrophage secretory mechanisms.

TMED10 regulates HFD-induced metabolic inflammation

Our previous work identified a non-lytic IL-1β release pathway, termed TMED10-channeled unconventional secretion (THU), in which TMED10 forms a protein translocator that mediates IL-1β transport into the ER–Golgi intermediate compartment for vesicular secretion[28,29]. To explore its role in metabolic inflammation, we generated *Lyz2*–cre *TMED10*$^{fl/fl}$ mice with myeloid lineage–specific TMED10 deletion and subjected them to HFD feeding to induce obesity (Extended Data Fig. 1a). Notably, despite comparable body weight gain and fat mass between TMED10-deficient and control (*TMED10*$^{fl/fl}$) mice (Extended Data Fig. 1a,b), macrophage TMED10 depletion resulted in an approximately 50% reduction in plasma IL-1β levels following HFD-induced obesity (Fig. 1i). HFD-driven macrophage accumulation in eWAT was markedly attenuated in TMED10-deficient mice, as evidenced by fewer CLSs and reduced adipose tissue macrophages detected by immunostaining and flow cytometric analysis (Fig. 1j-l). Importantly, these changes occurred independently of total fat mass, adipose depot distribution, adipocyte hypertrophy and white blood cell constitution (Extended Data Fig. 1b-e), highlighting a specific role of TMED10 in regulating the inflammatory response of ATMs during obesity. Consistently, transcriptomic profiling of obese adipose tissue further confirmed that macrophage TMED10 depletion resulted in substantially altered adipose transcriptome (Fig. 1m), with a pronounced repression of inflammatory gene expression (Fig. 1n,o, Extended Data Fig. 1f and Supplementary Table 2).

Of note, genes involved in adipose metabolic elasticity[30], adipogenesis, and fatty acid metabolism were upregulated in eWAT (Fig. 1p,q, Extended Data Fig. 1g and Supplementary Table 2), suggesting a metabolically healthier phenotype in obese TMED10-deficient mice. In agreement, insulin signaling was more robustly activated in obese eWAT of TMED10-deficient mice (Fig. 1r). Beyond adipose tissue, livers of obese TMED10-deficient mice exhibited reduced weight, alleviated hepatic steatosis, and diminished lipid accumulation (Extended Data Fig. 2a-d). Liver transcriptomic profiling revealed broad alterations, including downregulation of genes associated with inflammation and lipid synthesis (Extended Data Fig. 2e-g and Supplementary Table 3), alongside enhanced Akt phosphorylation in response to insulin stimulation (Extended Data Fig. 2h).

Relative to controls, HFD-fed *Lyz2*–cre *TMED10*$^{fl/fl}$ mice displayed reduced plasma glycerol and non-esterified fatty acid levels (Fig. 1s), as well as improved glucose tolerance and insulin sensitivity (Fig. 1t), reflecting enhanced systemic metabolic health upon macrophage TMED10 deficiency. Together, these findings demonstrate that myeloid lineage TMED10 promotes HFD-induced metabolic inflammation and systemic metabolic dysfunction, whereas its loss confers both metabolic and inflammatory protection.

IL-1β is the major pro-inflammatory cytokine accounting for the effect of TMED10 deficiency

IL-1β is a key pro-inflammatory cytokine produced by macrophages, and its release is regulated by TMED10[29,31]. Previous work indicated a direct involvement of IL-1β in insuslin resistance[32,33]. Pharmacological inhibition of IL-1β signaling in control (*TMED10*$^{fl/fl}$) mice using the IL-1 receptor antagonist (IL-1RA)[34] resulted in a comparable reduction of macrophage infiltration and CLSs in adipose tissue after HFD treatment as observed in *Lyz2*–cre *TMED10*$^{fl/fl}$ mice (Extended Data Fig. 3a). Moreover, the combination of IL-1RA treatment and TMED10 deficiency did not produce additional effects, indicating that TMED10 and IL-1β act within the same inflammatory pathway (Extended Data Fig. 3a).

Consistently, IL-1RA administration in control mice enhanced Akt phosphorylation in both adipose tissue and liver (Extended Data Fig. 3b,c), reduced hepatic lipid accumulation (Extended Data Fig. 3d-f), and improved systemic glucose metabolism as assessed by GTT and ITT (Extended Data Fig. 3g), to a similar extent as in *Lyz2*–cre *TMED10*$^{fl/fl}$ mice. Again, combined IL-1RA treatment in *Lyz2*–cre *TMED10*$^{fl/fl}$ mice did not further improve metabolic parameters (Extended Data Fig. 3b-g). A similar protective effect of IL-1RA against hyperglycermia was also reported before, supporting our conclusion[35].

Together, these findings demonstrate that TMED10-mediated IL-1β release is a principal contributor to HFD-induced metabolic inflammation and associated metabolic defects in our system.

Coupling of lipid uptake, sphingomyelin metabolism, and IL-1β release in a specialized macrophage subtype

Given that the metabolically detrimental effects of macrophage TMED10 were most evident in obesity, we asked whether TMED10 participates in the metabolic rewiring of ATMs upon HFD feeding, particularly with respect to lipid metabolism. As expected, multiple lipid metabolic pathways were substantially altered in ATMs from mice under varying durations of HFD feeding, based on previously published single-cell transcriptomic data[11] (Fig. 2a and Extended Data Fig. 4a-c). Genes involved in fatty acid, triglyceride, and general lipid metabolism were progressively upregulated with increasing HFD exposure (Fig. 2a). Notably, sphingolipid and glycosphingolipid metabolism in ATMs were markedly amplified in ATMs from long-term HFD-fed mice, whereas pathways related to overall phospholipid metabolism showed the opposite trend (Fig. 2a), suggesting a specific contribution of sphingolipid pathways to metabolic dysfunction. Remarkably, genes linked to sphingomyelin (SM, a major sphingolipid) metabolism, lipid uptake, and TMED10-regulated unconventional secretion (including *Tmed10*, *Rab1a*, *Rab1b*, and *Rab2a*[28]) exhibited strong co-upregulation in adipose macrophages following HFD treatment (Fig. 2b), indicating functional interplay between SM metabolism and TMED10 activity in inflammatory ATMs. We next focused on sphingolipid metabolism, as glycosphingolipid pathways were later found not to influence IL-1β release (see below).

Although a growing body of work has connected lipid metabolic rewiring to functional remodeling of heterogenous ATMs in the context of obesity[11-18,36], the mechnistic link between lipid metabolism and macrophage activation, particularly inflammatory responses, remains

unclear. To address this, we examined macrophage heterogeneity in lean and obese adipose tissue, and identified four major subtypes (Cluster 1-4) in eWAT based on transcriptomic features (Fig. 2c-g and Extended Data Fig. 4d, e). Cluster 1 corresponds to a resident macrophage population enriched for phagocytic markers (e.g., *Lyz2*) and exhibiting intermediate expression of lipid-uptake genes such as *Cd36* and *Trem2* (Fig. 2g and Extended Data Fig. 4d) suggesting a lipid-associated macrophage (LAM)-like subset. Cluster 2 comprises a perivascular macrophage population characterized by high expression of *Lyve1* and *Cd163*[13,36] (Extended Data Fig. 4d). Cluster 3 represents a LAM subset with elevated expression of lipid-metabolic genes (e.g., *Fabp4, Fabp5*) together with the highest levels of lipid-uptake markers (*Cd36, Trem2*)[11] (Fig. 2g and Extended Data Fig. 4d). Cluster 4 defines a proliferative macrophage population marked by robust *Mki67* expression (Extended Data Fig. 4d). Importantly, Cluster 3--predominantly detected in eWAT after long-term HFD feeding--exhibited co-enrichment of SM metabolism, lipid uptake, and TMED10-pathway genes, accompanied by a pronounced inflammatory gene signature (Fig. 2d-g and Extended Data Fig. 4e). Spatial transcriptomic analysis[12] further revealed that Cluster 3 macrophages localized primarily proximal to CLSs in adipose tissue (Fig. 2h), reinforcing their identity as a lipid-laden, pro-inflammatory cells. Collectively, these data indicate that Cluster 3 macrophages represent a LAM subtype that mediates lipid uptake and drives metabolic inflammation, which we term metabolic inflammation macrophages (MIM). Importantly, consistent with the observations in mouse, we identified an analogous MIM cluster in obese human visceral adipose tissue[13], characterized by elevated inflammatory signatures and co-upregulation of SM metabolism, lipid uptake, and TMED10-pathway genes (Fig. 2i-m and Extended Data Fig. 4f-i), suggesting conservation of this macrophage subtype across species.

Sphingomyelin regulates TMED10-dependent IL-1β release

Our above findings reveal a coordinated link among SM metabolism, lipid uptake, and TMED10-dependent IL-1β secretion within a specific inflammatory macrophage subtype, highlighting a potential mechanistic axis underlying metabolic inflammation.

To investigate the role of lipid uptake and SM metabolism in TMED10-mediated IL-1β release, we treated peritoneal macrophages with palmitic acid (PA) to mimic lipid uptake–induced inflammation in vivo[37-39]. PA stimulation induced IL-1β release, which was markedly reduced in TMED10-deficient macrophages but not in GSDMD-deficient cells, indicating that TMED10, rather than GSDMD, mediates PA-induced IL-1β secretion (Fig. 3a-d).

We next examined the role of SM biosynthesis using pharmacological inhibitors and genetic approaches (Fig. 3e)[40-43]. In macrophages, inhibition of SM synthase (by Malabaricone C, Mal C) or ceramide transport protein CERT (by HPA-12) efficiently suppressed PA-induced IL-1β release, comparable to inhibition of the inflammasome (by MCC950[44]) or caspase-1 (by Ac-YVAD-cmk)[45] (Fig. 3f). Although TMED10 deficiency already reduced IL-1β secretion, SM pathway inhibitors further decreased cytokine release (Fig. 3f), likely reflecting incomplete depletion of TMED10 in these cells (Fig. 3a). To clarify whether SM synthesis and TMED10 act in the same pathway, we generated TMED10-knockout THP-1 cells. In this model, SM synthesis inhibitors still blocked IL-1β release, but no further reduction was observed in TMED10-deficient cells, confirming that SM metabolism and TMED10 function within the same regulatory axis

(Fig. 3g-i). In contrast, inhibition of glycosphingolipid synthesis with Eliglustat[46] had no effect, excluding glycosphingolipids from this process (Fig. 3j).

IL-1β release involves two steps: inflammasome-dependent maturation and subsequent transport for secretion[47]. To test whether SM acts directly in the transport phase, we used a previously established HEK293T IL-1β secretion assay, in which mature IL-1β is expressed independently of inflammasome activation, allowing specific assessment of TMED10-dependent trafficking[28,29,48]. Exogenous SM treatment elevated cellular SM levels and significantly enhanced IL-1β release (Fig. 3k,l), whereas SM synthesis inhibitors (Mal C and HPA-12) but not glycosphingolipid synthesis inhibitor Eliglustat suppressed TMED10-mediated secretion (Fig. 3m,n).

Consistently, blocking SM degradation with the sphingomyelinase (SMPD2) inhibitor GW4869[49] increased both SM levels and IL-1β release (Fig. 3o,p). Genetic knockdown of SMPD2 produced similar results, while depletion of SGMS1, SGMS2, or CERT lowered SM levels and attenuated IL-1β secretion (Fig. 3q-s). Conversely, overexpression of SGMS1 or SMPD2 respectively increased or decreased SM abundance, leading to corresponding changes in IL-1β release (Fig. 3t,u).

Together, these findings demonstrate that SM is a key regulator of TMED10-dependent IL-1β secretion, acting downstream of inflammasome activation to control the transport and release of mature IL-1β.

TMED10 functions as a metabolic sensor activated by medium-chain sphingomyelin

To determine whether SM directly activates TMED10, we employed an established *in vitro* translocation assay[29] using TMED10-reconstituted proteoliposomes composed of phosphatidylcholine supplemented with various lipids (Fig. 4a). Among all lipids tested, only SM markedly enhanced TMED10-mediated IL-1β translocation (Fig. 4b,c and Extended Data Fig. 5a-e). In contrast, ceramide, a biosynthetic precursor of SM, inhibited TMED10 activity (Fig. 4c and Extended Data Fig. 5e). Consistently, hydrolysis of SM by sphingomyelinase abolished its enhancing effect (Fig. 4d,e). Furthermore, substitution of the choline head group with ethanolamine (ceramide phosphoethanolamine, CPE[50]) dramatically reduced TMED10 activity, demonstrating that TMED10 specifically responds to SM to promote protein translocation (Fig. 4f and Extended Data Fig. 5f).

Lipidomic profiling of adipose tissue macrophages from ND and HFD feeding mice revealed that phosphatidylglycerol and triglycerides increased as expected, whereas total SM level was unexpectly slightly decreased (Fig. 4g,h and Supplementary Table 4). However, a compositional shift was observed within the SM pool: medium-chain SM species (C16:0, C18:0) were elevated, whereas long-chain SM (C24:0) declined (Fig. 4i and Supplementary Table 4). Importantly, functional analysis of SM species in the *in vitro* translocation assay showed that medium-chain SM specifically activated TMED10, with an EC_{50} of approximately 0.5% and maximal activation near 1% (Fig. 4j-m and Extended Data Fig. 5g,h). These results indicate TMED10 as a highly sensitive and specific sensor of medium-chain SM, linking lipid remodeling under HFD conditions to TMED10 activation and IL-1β release in metabolic inflammation.

Sphingomyelin activates TMED10 through direct binding and oligomerization

To elucidate how SM activates TMED10, we first examined TMED10 homo-oligomerization, a hallmark of its translocator activity[29]. In a proximity ligation assay, overexpression of SGMS1 (an SM synthase) enhanced TMED10 self-association, whereas SMPD2 (a sphingomyelinase) reduced it, indicating a positive correlation between SM levels and TMED10 oligomerization (Fig. 5a,b). Consistently, cross-linking experiments revealed that SGMS1 increased, while SMPD2 decreased, the formation of high–molecular weight TMED10 complexes (Fig. 5c,d). Reconstitution experiments further demonstrated that the presence of SM in TMED10 proteoliposomes promoted oligomerization, which was reversed by sphingomyelinase treatment, indicating a direct role of SM on TMED10 activation (Fig. 5e,f).

In vivo, adipose tissue macrophages from HFD–fed mice displayed elevated TMED10 oligomer levels, consistent with increased activation (Fig. 5g,h). Similarly, PA treatment enhanced TMED10 oligomerization in macrophages, which was abolished by SM synthesis inhibition (Fig. 5i,j). These findings demonstrate that SM activates TMED10 by promoting its oligomer formation into an active translocator complex.

To assess whether SM directly interacts with TMED10, we performed lipid–protein pull-down assays and detected a specific association between TMED10 and SM (Fig. 5k). To define the interaction residues, we carried out molecular dynamics simulations using the TMED10 transmembrane domain (TMD) embedded in an SM-containing lipid bilayer (Supplementary Video 1). These simulations identified three residues—L197, L200, and Q204—as recurrent contact points for SM (Fig. 5l,m). Functional mutagenesis demonstrated that Q204, rather than L197 or L200, is essential for SM-dependent regulation of IL-1β secretion (Fig. 5n,o). We therefore selected the Q204L mutant for further analysis. Although Q204L did not alter TMED10 localization (Extended Data Fig. 6a), it abolished SM binding (Fig. 5p) and eliminated SM-induced oligomerization (Fig. 5q,r) and IL-1β translocation activity (Fig. 5s,t). These results indicate that Q204 plays a direct and indispensable role in sphingomyelin binding.

TMED10 sphingomyelin sensing governs metabolic inflammation

To investigate the physiological significance of TMED10-mediated SM sensing, we generated *TMED10*$^{Q204L/Q204L}$ knock-in mice (Extended Data Fig. 6b), in which a single amino acid substitution disrupts SM binding without altering TMED10 expression or its localization to the ERGIC in macrophages (Extended Data Fig. 6c,d). Despite normal localization, macrophages from *TMED10*$^{Q204L/Q204L}$ mice displayed a dramatic reduction in PA–induced IL-1β release, comparable to that observed in TMED10-deficient (*Lyz2*–Cre *TMED10*$^{fl/fl}$) macrophages (Fig. 6a). These findings underscore the critical role of SM sensing in TMED10-dependent IL-1β secretion.

To further assess the in vivo relevance, we performed bone marrow transplantation (BMT) experiments using WT, myeloid TMED10-KO (*Lyz2*–Cre *TMED10*$^{fl/fl}$), and TMED10-Q204L knock-in (*TMED10*$^{Q204L/Q204L}$) donor cells, followed by HFD treatment of irradiated myeloid TMED10-KO recipient mice (Fig. 6b,c). Notably, mice reconstituted with TMED10-Q204L knock-in bone marrow phenocopied TMED10-KO recipients, exhibiting significantly lower plasma IL-1β levels, reduced adipose tissue inflammation as shown by histological analysis and inflammatory gene expression (Fig. 6d-i, Extended Data Fig. 7a and Supplementary Table 5). Correspondingly, metabolic elastic genes as well as genes for adipogenesis and fatty acid

metabolism were increased (Fig. 6h,i, Extended Data Fig. 7b and Supplementary Table 5). Adipose insulin signaling is improved as indicated by enhanced Akt phosphorylation (Fig. 6j). In addition, the TMED10-Q204L transplants also phenocopied TMED10-KO recipients with increased insulin signaling and reduced lipid accumulation in liver (Extended Data Fig. 7c-e). Consistent with reduced metabolic inflammation, TMED10-Q204L bone marrow–transplanted mice showed improved systemic glucose tolerance (GTT) and insulin sensitivity (ITT) comparable to TMED10-KO transplants (Fig. 6k).

Together, these results demonstrate that sphingomyelin sensing by TMED10 is essential for macrophage-mediated metabolic inflammation, and that disruption of this lipid–protein interaction confers protection against HFD-induced inflammatory and metabolic dysfunction.

Discussion

It has been shown that ATMs gradually transition into a metabolically activated state during obesity[51-53]. These metabolically activated macrophages—largely corresponding to LAMs—accumulate lipids from diverse sources, including free lipids[54,55], exosomes[56], and dying adipocytes[57]. LAMs exert dual functions in obese adipose tissue. On one hand, they mediate lipid uptake, storage, and hydrolysis, thereby acting as a lipid-buffering system that helps maintain adipose tissue homeostasis[11,58,59]. On the other hand, LAMs can acquire pro-inflammatory features that contribute to insulin resistance[12,13,16]. Consistent with their homeostatic role, global deletion of *Trem2*, a central lipid receptor in LAMs, largely abolishes LAM function by impairing lipid uptake, leading to adipocyte hypotrophy and exacerbated metabolic dysfunction[11,58,60]. These findings suggest that, rather than eliminating LAMs, selectively inhibiting their pro-inflammatory activation may offer a more rational therapeutic strategy for ameliorating metabolic disease.

Our study identifies a TMED10–SM lipid-sensing pathway that governs metabolic inflammation in a specific LAM subset—MIM—which is a key driver of metabolic syndrome in obesity. In contrast to the canonical GSDMD-dependent inflammasome pathway that triggers acute, high-amplitude IL-1β release via pore formation, the TMED10–SM axis mediates a chronic, low-grade IL-1β secretion through the THU unconventional secretion pathway likely followed by GRASP55-mediated trafficking[61]. This mechanism is tightly coupled to lipid remodeling under metabolic stress, which generates bioactive SM species that directly bind TMED10 and initiate persistent inflammatory signaling (Fig. 6l).

The exceptional sensitivity of TMED10 to SM (EC_{50} ~0.5%) is physiologically significant. Given that most SM is synthesized in the Golgi[62], while the ERGIC, the site of TMED10 activity, contains minimal SM, this system allows precise detection of subtle fluctuations in local lipid composition. This principle is reminiscent of cholesterol sensing in the ER, where cholesterol level is low and ~5% cholesterol is the threshold to control SCAP–SREBP trafficking[63,64], highlighting a broader paradigm of highly sensitive lipid-sensing systems within the secretory pathway.

Notably, the SM-sensing glutamine (Q) residue is conserved across TMED family members[65], suggesting that TMED10's mechanism may extend to other TMED-mediated unconventional secretion pathways, consistent with reports of TMED2 binding SM[66]. Functionally, TMED10-SM

sensing acts as a molecular hub initiating chronic metabolic inflammation, with broader implications for disorders associated with lipid accumulation or sphingolipid dysregulation, including neurodegeneration, atherosclerosis, cancer, and metabolic dysfunction-associated steatohepatitis (MASH)[8,67-69]. These findings raise the intriguing possibility that targeting the TMED10–SM axis could modulate chronic inflammatory states more selectively than conventional anti-inflammatory approaches, offering a novel therapeutic avenue for metabolic and lipid-associated diseases.

Acknowledgement

The work is funded by National Natural Science Foundation of China (32225013, 32130023, 92254302, 32530024, 32450388, 32370728, 32571287, 82270926, 32241008) to L. Ge, B. Shan and M Zhang, National Key R&D Program of China (2025YFA0923003; 2024YFA1802600; 2021YFA0804802; 2022YFA1104102) to L. Ge, B. Shan and M Zhang, Tsinghua University Dushi Program, New Cornerstone Science Foundation.

We thank Dr. Feng Shao (National Institute of Biological Sciences, China), Dr. Bao-Liang Song (Wuhan University), Dr. Yong-Qiang Deng (South Medical University, China), Dr. Xiao-Yu Hu, Dr. Jing-Ren Zhang, Dr. Sen-Fang Sui and Dr. Shan Sun, Dr. Hai-Sha Liang (Tsinghua University) for materials and reagents. We thank Dr. Ye-Guang Chen and Dr. Li Yu (Tsinghua University) for helpful suggestions on the study. We thank Li-Na Xu and Yu-Pei Jiao at Facility center of Metabolomics and lipidomics in Tsinghua University for their help with the LC-MS/MS experiments.

Author contributions

M.Z., B.S. and L.G. conceptualized the study. J.Z., C.X., Z.W., T.Y., H.W., M.Z., B.S. and L.G. conceived the experiments and wrote the manuscript. J.Z., H.W. and D.P. carried out the cell biology and biochemistry experiments. C.X., Z.W., K.Z., Y.L. and F.C. performed mouse and primary cell experiments. T.Y. and Z.Q. analyed and visualized the RNA-seq data. X.L. performed the molecular dynamics simulation assay. M.Z., B.S. and L.G. supervised the project and provided funding.

Competing interests

Authors declare that they have no competing interests.

Supplemental information

Supplementary Table 1. Bulk RNA-seq data of eWAT from *GSDMD*$^{fl/fl}$ and *Lyz2*–cre *GSDMD*$^{fl/fl}$ mice after HFD feeding for 12 weeks.

Supplementary Table 2. Bulk RNA-seq data of eWAT from *TMED10*$^{fl/fl}$ and *Lyz2*–cre *TMED10*$^{fl/fl}$ mice after HFD feeding for 12 weeks.

Supplementary Table 3. Bulk RNA-seq data of liver from *TMED10*$^{fl/fl}$ and *Lyz2*–cre *TMED10*$^{fl/fl}$ mice after HFD feeding for 12 weeks.

Supplementary Table 4. Lipidomics analysis of ATMs from ND and HFD feeding mice.

Supplementary Table 5. Bulk RNA-seq data of eWAT from KO (*Lyz2*-cre *TMED10*$^{fl/fl}$) mice

transplanted with bone marrows of WT (*TMED10*$^{fl/fl}$), KO (Lyz2-cre *TMED10*$^{fl/fl}$) or Q204L knock-in (*TMED10*$^{Q204L/Q204L}$) mice after HFD feeding for 20 weeks.

Supplementary Table 6. Inflammatory response gene list for the quantification of inflammatory activity at the single-cell resolution.

Supplementary Video 1. Association between TMED10-TMD and SM in the lipid bilayer using molecular dynamics simulation. The video shows the movement of SM and TMED10 transmembrane region (colored in gray) with Q204 (colored in red) highlighted and PC hidden. SM was colored green (cytoplasmic face) and blue (luminal face) respectively.

References

1 Lingvay, I., Cohen, R. V., Roux, C. W. L. & Sumithran, P. Obesity in adults. *Lancet* **404**, 972-987, doi:10.1016/S0140-6736(24)01210-8 (2024).

2 Tilg, H., Ianiro, G., Gasbarrini, A. & Adolph, T. E. Adipokines: masterminds of metabolic inflammation. *Nat Rev Immunol* **25**, 250-265, doi:10.1038/s41577-024-01103-8 (2025).

3 Chavakis, T., Alexaki, V. I. & Ferrante, A. W., Jr. Macrophage function in adipose tissue homeostasis and metabolic inflammation. *Nat Immunol* **24**, 757-766, doi:10.1038/s41590-023-01479-0 (2023).

4 Kawai, T., Autieri, M. V. & Scalia, R. Adipose tissue inflammation and metabolic dysfunction in obesity. *Am J Physiol Cell Physiol* **320**, C375-C391, doi:10.1152/ajpcell.00379.2020 (2021).

5 Cypess, A. M. Reassessing Human Adipose Tissue. *N Engl J Med* **386**, 768-779, doi:10.1056/NEJMra2032804 (2022).

6 Hotamisligil, G. S. Inflammation, metaflammation and immunometabolic disorders. *Nature* **542**, 177-185, doi:10.1038/nature21363 (2017).

7 Saltiel, A. R. & Olefsky, J. M. Inflammatory mechanisms linking obesity and metabolic disease. *J Clin Invest* **127**, 1-4, doi:10.1172/JCI92035 (2017).

8 Hagberg, C. E. & Spalding, K. L. White adipocyte dysfunction and obesity-associated pathologies in humans. *Nat Rev Mol Cell Biol* **25**, 270-289, doi:10.1038/s41580-023-00680-1 (2024).

9 Shaikh, S. R., Beck, M. A., Alwarawrah, Y. & MacIver, N. J. Emerging mechanisms of obesity-associated immune dysfunction. *Nat Rev Endocrinol* **20**, 136-148, doi:10.1038/s41574-023-00932-2 (2024).

10 Crewe, C., An, Y. A. & Scherer, P. E. The ominous triad of adipose tissue dysfunction: inflammation, fibrosis, and impaired angiogenesis. *J Clin Invest* **127**, 74-82, doi:10.1172/JCI88883 (2017).

11 Jaitin, D. A. *et al.* Lipid-Associated Macrophages Control Metabolic Homeostasis in a Trem2-Dependent Manner. *Cell* **178**, 686-698 e614, doi:10.1016/j.cell.2019.05.054 (2019).

12 Stansbury, C. M. *et al.* A lipid-associated macrophage lineage rewires the spatial landscape of adipose tissue in early obesity. *JCI Insight* **8**, doi:10.1172/jci.insight.171701 (2023).

13 Hildreth, A. D. *et al.* Single-cell sequencing of human white adipose tissue identifies new cell states in health and obesity. *Nat Immunol* **22**, 639-653, doi:10.1038/s41590-021-00922-4 (2021).

14 Coats, B. R. *et al.* Metabolically Activated Adipose Tissue Macrophages Perform Detrimental

and Beneficial Functions during Diet-Induced Obesity. *Cell Rep* **20**, 3149-3161, doi:10.1016/j.celrep.2017.08.096 (2017).

15 Dib, L. *et al.* Lipid-associated macrophages transition to an inflammatory state in human atherosclerosis increasing the risk of cerebrovascular complications. *Nat Cardiovasc Res* **2**, 656-672, doi:10.1038/s44161-023-00295-x (2023).

16 Dahik, V. D. *et al.* ABCG1 orchestrates adipose tissue macrophage plasticity and insulin resistance in obesity by rewiring saturated fatty acid pools. *Sci Transl Med* **16**, eadi6682, doi:10.1126/scitranslmed.adi6682 (2024).

17 Miranda, A. M. A. *et al.* Selective remodelling of the adipose niche in obesity and weight loss. *Nature* **644**, 769-779, doi:10.1038/s41586-025-09233-2 (2025).

18 Hill, D. A. *et al.* Distinct macrophage populations direct inflammatory versus physiological changes in adipose tissue. *Proc Natl Acad Sci U S A* **115**, E5096-E5105, doi:10.1073/pnas.1802611115 (2018).

19 Kayagaki, N. *et al.* Caspase-11 cleaves gasdermin D for non-canonical inflammasome signalling. *Nature* **526**, 666-671, doi:10.1038/nature15541 (2015).

20 Shi, J. *et al.* Cleavage of GSDMD by inflammatory caspases determines pyroptotic cell death. *Nature* **526**, 660-665, doi:10.1038/nature15514 (2015).

21 Evavold, C. L. *et al.* The Pore-Forming Protein Gasdermin D Regulates Interleukin-1 Secretion from Living Macrophages. *Immunity* **48**, 35-44 e36, doi:10.1016/j.immuni.2017.11.013 (2018).

22 Ding, J. *et al.* Pore-forming activity and structural autoinhibition of the gasdermin family. *Nature* **535**, 111-116, doi:10.1038/nature18590 (2016).

23 Stienstra, R. *et al.* The inflammasome-mediated caspase-1 activation controls adipocyte differentiation and insulin sensitivity. *Cell Metab* **12**, 593-605, doi:10.1016/j.cmet.2010.11.011 (2010).

24 Vandanmagsar, B. *et al.* The NLRP3 inflammasome instigates obesity-induced inflammation and insulin resistance. *Nat Med* **17**, 179-188, doi:10.1038/nm.2279 (2011).

25 Saberi, M. *et al.* Hematopoietic cell-specific deletion of toll-like receptor 4 ameliorates hepatic and adipose tissue insulin resistance in high-fat-fed mice. *Cell Metab* **10**, 419-429, doi:10.1016/j.cmet.2009.09.006 (2009).

26 Rathkey, J. K. *et al.* Chemical disruption of the pyroptotic pore-forming protein gasdermin D inhibits inflammatory cell death and sepsis. *Sci Immunol* **3**, doi:10.1126/sciimmunol.aat2738 (2018).

27 Hu, J. J. *et al.* FDA-approved disulfiram inhibits pyroptosis by blocking gasdermin D pore formation. *Nat Immunol* **21**, 736-745, doi:10.1038/s41590-020-0669-6 (2020).

28 Sun, Y. *et al.* A dual role of ERGIC-localized Rabs in TMED10-mediated unconventional protein secretion. *Nat Cell Biol* **26**, 1077-1092, doi:10.1038/s41556-024-01445-4 (2024).

29 Zhang, M. *et al.* A Translocation Pathway for Vesicle-Mediated Unconventional Protein Secretion. *Cell* **181**, 637-652 e615, doi:10.1016/j.cell.2020.03.031 (2020).

30 Zhou, Q., Yu, L., Cook, J. R., Qiang, L. & Sun, L. Deciphering the decline of metabolic elasticity in aging and obesity. *Cell Metab* **35**, 1661-1671 e1666, doi:10.1016/j.cmet.2023.08.001 (2023).

31 Liu, L. *et al.* Coronavirus envelope protein activates TMED10-mediated unconventional secretion of inflammatory factors. *Nat Commun* **15**, 8708, doi:10.1038/s41467-024-52818-0 (2024).

32 Jager, J., Gremeaux, T., Cormont, M., Le Marchand-Brustel, Y. & Tanti, J. F. Interleukin-1beta-

induced insulin resistance in adipocytes through down-regulation of insulin receptor substrate-1 expression. *Endocrinology* **148**, 241-251, doi:10.1210/en.2006-0692 (2007).

33 Lumeng, C. N., Deyoung, S. M. & Saltiel, A. R. Macrophages block insulin action in adipocytes by altering expression of signaling and glucose transport proteins. *Am J Physiol Endocrinol Metab* **292**, E166-174, doi:10.1152/ajpendo.00284.2006 (2007).

34 Broderick, L. & Hoffman, H. M. IL-1 and autoinflammatory disease: biology, pathogenesis and therapeutic targeting. *Nat Rev Rheumatol* **18**, 448-463, doi:10.1038/s41584-022-00797-1 (2022).

35 Sauter, N. S., Schulthess, F. T., Galasso, R., Castellani, L. W. & Maedler, K. The antiinflammatory cytokine interleukin-1 receptor antagonist protects from high-fat diet-induced hyperglycemia. *Endocrinology* **149**, 2208-2218, doi:10.1210/en.2007-1059 (2008).

36 Sarvari, A. K. *et al.* Plasticity of Epididymal Adipose Tissue in Response to Diet-Induced Obesity at Single-Nucleus Resolution. *Cell Metab* **33**, 437-453 e435, doi:10.1016/j.cmet.2020.12.004 (2021).

37 Korbecki, J. & Bajdak-Rusinek, K. The effect of palmitic acid on inflammatory response in macrophages: an overview of molecular mechanisms. *Inflamm Res* **68**, 915-932, doi:10.1007/s00011-019-01273-5 (2019).

38 Snodgrass, R. G., Huang, S., Choi, I. W., Rutledge, J. C. & Hwang, D. H. Inflammasome-mediated secretion of IL-1beta in human monocytes through TLR2 activation; modulation by dietary fatty acids. *J Immunol* **191**, 4337-4347, doi:10.4049/jimmunol.1300298 (2013).

39 Wen, H. *et al.* Fatty acid-induced NLRP3-ASC inflammasome activation interferes with insulin signaling. *Nat Immunol* **12**, 408-415, doi:10.1038/ni.2022 (2011).

40 Quinville, B. M., Deschenes, N. M., Ryckman, A. E. & Walia, J. S. A Comprehensive Review: Sphingolipid Metabolism and Implications of Disruption in Sphingolipid Homeostasis. *Int J Mol Sci* **22**, doi:10.3390/ijms22115793 (2021).

41 Adada, M., Luberto, C. & Canals, D. Inhibitors of the sphingomyelin cycle: Sphingomyelin synthases and sphingomyelinases. *Chem Phys Lipids* **197**, 45-59, doi:10.1016/j.chemphyslip.2015.07.008 (2016).

42 Othman, M. A. *et al.* Malabaricone C as Natural Sphingomyelin Synthase Inhibitor against Diet-Induced Obesity and Its Lipid Metabolism in Mice. *ACS Med Chem Lett* **10**, 1154-1158, doi:10.1021/acsmedchemlett.9b00171 (2019).

43 Hanada, K., Sakai, S. & Kumagai, K. Natural Ligand-Mimetic and Nonmimetic Inhibitors of the Ceramide Transport Protein CERT. *Int J Mol Sci* **23**, doi:10.3390/ijms23042098 (2022).

44 Coll, R. C. *et al.* A small-molecule inhibitor of the NLRP3 inflammasome for the treatment of inflammatory diseases. *Nat Med* **21**, 248-255, doi:10.1038/nm.3806 (2015).

45 Pan, P. *et al.* SARS-CoV-2 N protein promotes NLRP3 inflammasome activation to induce hyperinflammation. *Nat Commun* **12**, 4664, doi:10.1038/s41467-021-25015-6 (2021).

46 Dong, L. *et al.* Inhibition of glycosphingolipid synthesis with eliglustat in combination with immune checkpoint inhibitors in advanced cancers: preclinical evidence and phase I clinical trial. *Nat Commun* **15**, 6970, doi:10.1038/s41467-024-51495-3 (2024).

47 Sitia, R. & Rubartelli, A. The unconventional secretion of IL-1beta: Handling a dangerous weapon to optimize inflammatory responses. *Semin Cell Dev Biol* **83**, 12-21, doi:10.1016/j.semcdb.2018.03.011 (2018).

48 Zhang, M., Kenny, S. J., Ge, L., Xu, K. & Schekman, R. Translocation of interleukin-1beta into a

vesicle intermediate in autophagy-mediated secretion. *Elife* **4**, e11205, doi:10.7554/eLife.11205 (2015).

49 Menck, K. *et al.* Neutral sphingomyelinases control extracellular vesicles budding from the plasma membrane. *J Extracell Vesicles* **6**, 1378056, doi:10.1080/20013078.2017.1378056 (2017).

50 Panevska, A., Skocaj, M., Krizaj, I., Macek, P. & Sepcic, K. Ceramide phosphoethanolamine, an enigmatic cellular membrane sphingolipid. *Biochim Biophys Acta Biomembr* **1861**, 1284-1292, doi:10.1016/j.bbamem.2019.05.001 (2019).

51 Xu, X. *et al.* Obesity activates a program of lysosomal-dependent lipid metabolism in adipose tissue macrophages independently of classic activation. *Cell Metab* **18**, 816-830, doi:10.1016/j.cmet.2013.11.001 (2013).

52 Kratz, M. *et al.* Metabolic dysfunction drives a mechanistically distinct proinflammatory phenotype in adipose tissue macrophages. *Cell Metab* **20**, 614-625, doi:10.1016/j.cmet.2014.08.010 (2014).

53 Luo, J. H. *et al.* PDIA3 defines a novel subset of adipose macrophages to exacerbate the development of obesity and metabolic disorders. *Cell Metab* **36**, 2262-2280 e2265, doi:10.1016/j.cmet.2024.08.009 (2024).

54 Nicholls, H. T. *et al.* Hematopoietic cell-restricted deletion of CD36 reduces high-fat diet-induced macrophage infiltration and improves insulin signaling in adipose tissue. *Diabetes* **60**, 1100-1110, doi:10.2337/db10-1353 (2011).

55 Kennedy, D. J. *et al.* A CD36-dependent pathway enhances macrophage and adipose tissue inflammation and impairs insulin signalling. *Cardiovasc Res* **89**, 604-613, doi:10.1093/cvr/cvq360 (2011).

56 Flaherty, S. E., 3rd *et al.* A lipase-independent pathway of lipid release and immune modulation by adipocytes. *Science* **363**, 989-993, doi:10.1126/science.aaw2586 (2019).

57 Cinti, S. *et al.* Adipocyte death defines macrophage localization and function in adipose tissue of obese mice and humans. *J Lipid Res* **46**, 2347-2355, doi:10.1194/jlr.M500294-JLR200 (2005).

58 Winn, N. C., Wolf, E. M., Garcia, J. N. & Hasty, A. H. Exon 2-mediated deletion of Trem2 does not worsen metabolic function in diet-induced obese mice. *J Physiol* **600**, 4485-4501, doi:10.1113/JP283684 (2022).

59 Xu, R. *et al.* Lipid-associated macrophages between aggravation and alleviation of metabolic diseases. *Trends Endocrinol Metab* **35**, 981-995, doi:10.1016/j.tem.2024.04.009 (2024).

60 Sharif, O. *et al.* Beneficial Metabolic Effects of TREM2 in Obesity Are Uncoupled From Its Expression on Macrophages. *Diabetes* **70**, 2042-2057, doi:10.2337/db20-0572 (2021).

61 Chiritoiu, M., Brouwers, N., Turacchio, G., Pirozzi, M. & Malhotra, V. GRASP55 and UPR Control Interleukin-1beta Aggregation and Secretion. *Dev Cell* **49**, 145-155 e144, doi:10.1016/j.devcel.2019.02.011 (2019).

62 Yamaji, T. & Hanada, K. Sphingolipid metabolism and interorganellar transport: localization of sphingolipid enzymes and lipid transfer proteins. *Traffic* **16**, 101-122, doi:10.1111/tra.12239 (2015).

63 Brown, M. S., Radhakrishnan, A. & Goldstein, J. L. Retrospective on Cholesterol Homeostasis: The Central Role of Scap. *Annu Rev Biochem* **87**, 783-807, doi:10.1146/annurev-biochem-062917-011852 (2018).

64 Radhakrishnan, A., Goldstein, J. L., McDonald, J. G. & Brown, M. S. Switch-like control of SREBP-

2 transport triggered by small changes in ER cholesterol: a delicate balance. *Cell Metab* **8**, 512-521, doi:10.1016/j.cmet.2008.10.008 (2008).

65 Pastor-Cantizano, N., Montesinos, J. C., Bernat-Silvestre, C., Marcote, M. J. & Aniento, F. p24 family proteins: key players in the regulation of trafficking along the secretory pathway. *Protoplasma* **253**, 967-985, doi:10.1007/s00709-015-0858-6 (2016).

66 Contreras, F. X. *et al.* Molecular recognition of a single sphingolipid species by a protein's transmembrane domain. *Nature* **481**, 525-529, doi:10.1038/nature10742 (2012).

67 Hannun, Y. A. & Obeid, L. M. Sphingolipids and their metabolism in physiology and disease. *Nat Rev Mol Cell Biol* **19**, 175-191, doi:10.1038/nrm.2017.107 (2018).

68 Haney, M. S. *et al.* APOE4/4 is linked to damaging lipid droplets in Alzheimer's disease microglia. *Nature* **628**, 154-161, doi:10.1038/s41586-024-07185-7 (2024).

69 Xiong, X. *et al.* Landscape of Intercellular Crosstalk in Healthy and NASH Liver Revealed by Single-Cell Secretome Gene Analysis. *Mol Cell* **75**, 644-660 e645, doi:10.1016/j.molcel.2019.07.028 (2019).

70 Ji, L. *et al.* Slc6a8-Mediated Creatine Uptake and Accumulation Reprogram Macrophage Polarization via Regulating Cytokine Responses. *Immunity* **51**, 272-284 e277, doi:10.1016/j.immuni.2019.06.007 (2019).

71 Xu, J., Pickard, J. M. & Nunez, G. FDA-approved disulfiram inhibits the NLRP3 inflammasome by regulating NLRP3 palmitoylation. *Cell Rep* **43**, 114609, doi:10.1016/j.celrep.2024.114609 (2024).

72 Zheng, J. *et al.* TMEDs mediate versatile cargo transport in vesicle-dependent unconventional secretion. *J Cell Biol* **225**, doi:10.1083/jcb.202503075 (2026).

73 Ma, X. *et al.* CCT2 is an aggrephagy receptor for clearance of solid protein aggregates. *Cell* **185**, 1325-1345 e1322, doi:10.1016/j.cell.2022.03.005 (2022).

74 Li, X. *et al.* Macrophage HIF-2alpha suppresses NLRP3 inflammasome activation and alleviates insulin resistance. *Cell Rep* **36**, 109607, doi:10.1016/j.celrep.2021.109607 (2021).

75 Matyash, V., Liebisch, G., Kurzchalia, T. V., Shevchenko, A. & Schwudke, D. Lipid extraction by methyl-tert-butyl ether for high-throughput lipidomics. *J Lipid Res* **49**, 1137-1146, doi:10.1194/jlr.D700041-JLR200 (2008).

76 Tang, H. *et al.* Establishment of local searching methods for orbitrap-based high throughput metabolomics analysis. *Talanta* **156-157**, 163-171, doi:10.1016/j.talanta.2016.04.051 (2016).

77 Xu, L., Wang, X., Jiao, Y. & Liu, X. Assessment of potential false positives via orbitrap-based untargeted lipidomics from rat tissues. *Talanta* **178**, 287-293, doi:10.1016/j.talanta.2017.09.046 (2018).

78 Ying, W. *et al.* Adipose Tissue Macrophage-Derived Exosomal miRNAs Can Modulate In Vivo and In Vitro Insulin Sensitivity. *Cell* **171**, 372-384 e312, doi:10.1016/j.cell.2017.08.035 (2017).

79 Subramanian, A. *et al.* Gene set enrichment analysis: a knowledge-based approach for interpreting genome-wide expression profiles. *Proc Natl Acad Sci U S A* **102**, 15545-15550, doi:10.1073/pnas.0506580102 (2005).

80 Yu, G., Wang, L. G., Han, Y. & He, Q. Y. clusterProfiler: an R package for comparing biological themes among gene clusters. *OMICS* **16**, 284-287, doi:10.1089/omi.2011.0118 (2012).

81 Liberzon, A. *et al.* The Molecular Signatures Database (MSigDB) hallmark gene set collection. *Cell Syst* **1**, 417-425, doi:10.1016/j.cels.2015.12.004 (2015).

82 Zheng, G. X. *et al.* Massively parallel digital transcriptional profiling of single cells. *Nat Commun*

8, 14049, doi:10.1038/ncomms14049 (2017).

83 Satija, R., Farrell, J. A., Gennert, D., Schier, A. F. & Regev, A. Spatial reconstruction of single-cell gene expression data. *Nat Biotechnol* **33**, 495-502, doi:10.1038/nbt.3192 (2015).

84 Stuart, T. *et al.* Comprehensive Integration of Single-Cell Data. *Cell* **177**, 1888-1902 e1821, doi:10.1016/j.cell.2019.05.031 (2019).

85 McGinnis, C. S., Murrow, L. M. & Gartner, Z. J. DoubletFinder: Doublet Detection in Single-Cell RNA Sequencing Data Using Artificial Nearest Neighbors. *Cell Syst* **8**, 329-337 e324, doi:10.1016/j.cels.2019.03.003 (2019).

86 Becht, E. *et al.* Dimensionality reduction for visualizing single-cell data using UMAP. *Nat Biotechnol*, doi:10.1038/nbt.4314 (2018).

87 Wu, Y. *et al.* Spatiotemporal Immune Landscape of Colorectal Cancer Liver Metastasis at Single-Cell Level. *Cancer Discov* **12**, 134-153, doi:10.1158/2159-8290.CD-21-0316 (2022).

88 Liberzon, A. *et al.* Molecular signatures database (MSigDB) 3.0. *Bioinformatics* **27**, 1739-1740, doi:10.1093/bioinformatics/btr260 (2011).

89 Kanehisa, M. & Goto, S. KEGG: kyoto encyclopedia of genes and genomes. *Nucleic Acids Res* **28**, 27-30, doi:10.1093/nar/28.1.27 (2000).

90 Hanzelmann, S., Castelo, R. & Guinney, J. GSVA: gene set variation analysis for microarray and RNA-seq data. *BMC Bioinformatics* **14**, 7, doi:10.1186/1471-2105-14-7 (2013).

91 Liang, H. *et al.* The formation of migrasomes is initiated by the assembly of sphingomyelin synthase 2 foci at the leading edge of migrating cells. *Nat Cell Biol* **25**, 1173-1184, doi:10.1038/s41556-023-01188-8 (2023).

92 Deng, Y., Rivera-Molina, F. E., Toomre, D. K. & Burd, C. G. Sphingomyelin is sorted at the trans Golgi network into a distinct class of secretory vesicle. *Proc Natl Acad Sci U S A* **113**, 6677-6682, doi:10.1073/pnas.1602875113 (2016).

93 Back, M. J. *et al.* Activation of neutral sphingomyelinase 2 by starvation induces cell-protective autophagy via an increase in Golgi-localized ceramide. *Cell Death Dis* **9**, 670, doi:10.1038/s41419-018-0709-4 (2018).

94 Varadi, M. *et al.* AlphaFold Protein Structure Database: massively expanding the structural coverage of protein-sequence space with high-accuracy models. *Nucleic Acids Res* **50**, D439-D444, doi:10.1093/nar/gkab1061 (2022).

95 Huang, J. *et al.* CHARMM36m: an improved force field for folded and intrinsically disordered proteins. *Nat Methods* **14**, 71-73, doi:10.1038/nmeth.4067 (2017).

96 Abraham, M. J. *et al.* GROMACS: High performance molecular simulations through multi-level parallelism from laptops to supercomputers. *SoftwareX* **1-2**, 19-25, doi:10.1016/j.softx.2015.06.001 (2015).

97 NosÉ, S. A molecular dynamics method for simulations in the canonical ensemble. *Molecular Physics* **100**, 191-198, doi:10.1080/00268970110089108 (2002).

98 Hoover, W. G. Canonical dynamics: Equilibrium phase-space distributions. *Phys Rev A Gen Phys* **31**, 1695-1697, doi:10.1103/physreva.31.1695 (1985).

99 Parrinello, M. & Rahman, A. Polymorphic Transitions in Single-Crystals - a New Molecular-Dynamics Method. *Journal of Applied Physics* **52**, 7182-7190, doi:10.1063/1.328693 (1981).

100 Humphrey, W., Dalke, A. & Schulten, K. VMD: visual molecular dynamics. *J Mol Graph* **14**, 33-38, 27-38, doi:10.1016/0263-7855(96)00018-5 (1996).

Methods

Mice

The mice experiments were approved by the Institutional Animal Care and Use Committees at Tsinghua University. Mice were housed in ventilated cages in a temperature and light regulated room in a SPF facility and received food and water *ad libitum*. *TMED10*$^{fl/fl}$ mice (C57BL/6J)[29] and *TMED10*$^{Q204L/Q204L}$ knock-in mice (C57BL/6J) were created using CRISPR-Cas9-mdiated targeting by GemPharmatech Co. Ltd, China. *GSDMD*$^{fl/fl}$ mice were originated from Dr. Feng Shao as previously described[20]. Mice with myeloid cell lineage-specific *GSDMD* or *TMED10* deletion were generated via crossbreeding with *Lyz2*-Cre mice (C57BL/6J)[70], a kind gift from Dr. Xiaoyu Hu lab at Tsinghua University. The genotyping primers were listed in **Extended Data Table 1**. TMED10-Q204L mutation was validated by DNA sequencing. Metabolic challenges were initiated in 6- to 8-week-old mice. Mice were fed either a standard chow diet (10% kcal from fat) or a high-fat diet (HFD, 60% kcal from fat; Research Diets D12492) for up to 20 weeks. Sepsis was induced in C57BL/6 male mice (8-12 weeks old) by intraperitoneal injection of 25 mg/kg LPS[27,71]. IL-1β in plasma and peritoneal lavage were measured by ELISA 12 hours after LPS challenge.

Cells

HEK293T, HeLa, U2OS cells (from Dr. Randy Schekman) were maintained in Dulbecco's modified Eagle's medium (DMEM) supplemented with 10% FBS at 37°C in 5% CO_2. THP-1 cells (from Dr. Gong Cheng) and primary peritoneal macrophages were maintained in RPMI-1640 supplemented with 10% FBS at 37°C in 5% CO_2. TMED10-KO HEK293T, TMED10-KO HeLa and TMED10-KO THP-1 cells were generated using CRISPR-cas9 system as reported previously[29,72]. For protein purification in mammalian cells, 293F cells (from Dr. Shan Sun and Dr. Sen-Fang Sui) were cultured in SMM293-TII (Sino Biological) at 37°C, 110 rpm with 5% CO_2.

Reagents and antibodies

We obtained proteinase K (P8044), Anti-FLAG agarose (A2220) and LPS (L4130, from Escherichia coli O111:B4) from sigma; protease inhibitor cocktail (11836145001) from Roche; Phorbol 12-myristate 13-acetate (PMA, HY-18739), MCC950 (HY-12815), Ac-YVAD-cmk (HY-16990) and Malabaricone C (Mal C, HY-N8518) from MCE; HPA-12 (H1553) from TCI; Eliglustat (S7852) and GW4869 (S7609) from Selleck; Tert-Butyl methyl ether (MTBE, B802535) from Macklin; Phenylmethylsulfonyl fluoride (PMSF; ST505) and BCA Protein Assay Kit (P0012S) from Beyotime; DDM (1758-1350) from Inalco; 3×FLAG peptide from GL Biochem; Optiprep (AS1114542) from Axis-Shield and DSS (21555) from Thermo. We purchased Ni NTA

Beads 6FF (SA005500) and Glutathione Beads 4FF (SA010500) from Smart-Lifesciences; Mouse IL-1β Precoated ELISA Kit (1210122), Human IL-1β Precoated ELISA Kit (1110122) from Dakewe Biotech; Mouse IL-1 beta ELISA Kit (KE10003) from proteintech.

We purchased mouse anti-V5 antibody (V8012; IF, 1:500) and mouse anti-FLAG antibody (F3165; WB, 1:5,000) from Sigma; rabbit anti-TMED10 antibody (15199-1-AP; WB, 1:2,000), mouse anti-TMED10 antibody (67876-1-Ig; IF, 1:200), rabbit anti-ERGIC53 antibody (13364-1-AP; IF, 1:200) and rabbit anti-CERT antibody (15191-1-AP; WB, 1:2,000) from Proteintech; rabbit anti-GSDMD antibody (Ab219800; WB, 1:2000), rat anti-F4/80 antibody (ab6640; ICC, 1:200; IF, 1:500) from Abcam; rabbit anti-AKT antibody (4691S, WB, 1:2000), rabbit anti phospho-Akt (Ser473) antibody (4060S, WB, 1:2000), rabbit anti-V5 antibody (13202; IF, 1:500; WB, 1:5,000), rabbit anti-HA antibody (3724; IF, 1:500; WB, 1:5,000) and mouse anti-GST antibody (2624; WB, 1:10,000) from CST; rat anti-HA from Chromotek (7C9; IF, 1:500); mouse anti-tubulin antibody (200608; WB, 1:10,000) and mouse anti-actin antibody (200068-8F10; WB, 1:5,000) from Zen Bioscience; mouse anti-ERGIC53 antibody (ENZ-ABS300-0100; WB, 1:4,000) from Enzo and mouse anti-T7 antibody (69522; WB, 1:5,000) from Novagen. Rabbit anti-TMED10 antibody (for endogenous TMED10 detection in DSS crosslink assay; WB, 1:2,000) were purified by ABclonal. Rabbit anti-RPN1 antibody (WB, 1:5,000) were originated from Dr. Randy Schekman and described previously[29,73].

Primary peritoneal macrophages separation

Primary peritoneal macrophages were separated as described previously[74]. In brief, mice were injected intraperitoneally with 2 mL of 4% thioglycollate broth medium (BD BBL, 211716). Three days later, peritoneal cells were collected in PBS containing 10% FBS. The collected cells were cultured in RPMI-1640 supplemented with 10% FBS, 100 units/ml penicillin, and 100 μg/ml streptomycin for 3 hours. Non-adherent cells were gently washed away with PBS. The adherent peritoneal macrophages were used for further experiments including IL-1β secretion detection or immunofluorescence analysis.

Isolation of stromal vascular fractions (SVF) and macrophages from eWAT

Epididymal white adipose tissues were collected and digested with DMEM/F12 (HYCLONE, sh30023.01) containing 1% BSA (Biodee, 100g-0332) and 1% collagenase I (Thermo, 17100017) at 37°C with shaking at 120 rpm for 30 min. After centrifugation at 500 x *g* for 10 min at 4°C, the SVF pellets were collected, filtered with 70 μm cell strainer, subjected to red blood cell lysis and resuspended in PBS containing 2% FBS and 2 mM EDTA for further experiments. To isolate adipose tissue macrophages (ATMs), F4/80+ macrophages were separated from the SVF with a MagniSort Mouse F4/80 Positive Selection Kit (Thermo, 8802-6863-74) according to the manufacturer's instructions.

Flow cytometry analysis

Cell suspensions prepared from the SVF were stained with indicated fluorescent-conjugated antibodies for 30 min at 4°C in the dark. The antibodies used for macrophage analysis included: F4/80-PE (CST, 64763S, 1:200), CD11b-eFluor 610 (eBioscience, 61-0112-80, 1:200) and Zombie NIR™ Fixable Viability Kit (BioLegend, 423105, 1:500). Samples were then subjected to flow cytometry analysis with BD LSRFortessa SORP (BD Biosciences). Data were analyzed using the FlowJo V10.8.1 software.

Lipidomics analysis

ATMs were prepared as above. To obtain similar cell numbers, ATMs from 6 mice on ND or 1 mouse on HFD for 12 weeks were pooled for one sample. For lipid extraction from ATMs, we used a modified methyl-tert-butyl ether (MTBE)/methanol method[75]. Briefly, cells were resuspended in 300 μL methanol and vortexed for 1 min. Then 1 mL MTBE was added and vortexed for 1 min. Then 250 μL H_2O was added and vortexed for 1 min. The mixture was allowed to stand for 5 min and vortex for 1min, which is repeated for 3 times. Then samples were centrifuged at 8,000 rpm for 15 min. The upper layer was collected and dried by nitrogen. Lipid samples were stored in −80°C freezer as dry pellets. Lipid pellets were re-dissolved in 150 μL dichloromethane/methanol (v:v=2:1) for LC-MS/MS.

LC-MS/MS method for lipid analysis was described previously[76,77] and performed at facility center of metabolomics and lipidomics in Tsinghua University. Briely, reverse phase chromatography was selected for LC separation using Cortecs C18 column (2.1*100 mm, 2.7μm, Waters). Mobile phase A was made by mixing 400 mL of HPLC-grade water containing 0.395 g of ammonium bicarbonate with 600 mL of HPLC-grade acetonitrile. Mobile phase B contained 10% ACN and 90% IPA (v/v). Gradient elution was performed at a flow rate of 0.28 mL/min, and the column oven temperature was set to 40°C. The gradient was as follow: 0 min, 30%B; 3.0 min, 30% B; 4.5 min, 33% B; 7.0 min, 45% B; 8.0 min, 52% B; 11.0 min, 58% B; 14.0 min, 66% B; 17.0 min, 70% B; 21.0 min, 75% B; 23.0 min, 98% B; 30.0 min, 98% B; 30.5 min, 30% B; 35.0 min, 30% B. Data was acquired using Orbitrap Exploris 240 mass spectrometer (Thermo, CA) coupled with UHPLC system Vanquish (Thermo, CA). The detailed mass spectrometer parameters were as follows: spray voltage, 3.2 kV for positive and 2.8 kV for negative; capillary temperature, 320 °C; sheath gas flow rate (arb),35; aux gas flow rate (arb),10; mass range(m/z), 240–2000 for positive and 200–2000 for negative. Full MS resolution, 60,000; MS/MS resolution, 15,000; NCE,15/30/45; duty cycle,1s.

For lipid identification, lipids were identified and quantified using LipidSearch 5.0 (Thermo Fisher, USA). Lipid Search v5.0 contains 18 lipid species and more than 1,500,000 fragment ions in the database. It allows lipid identification based on MS/MS match. Mass tolerance for

precursor and fragment was set to 8 ppm and 10 ppm respectively. The displayed m-score threshold was selected as 5 and grades A, B, C, D were all used for ID quality filter. All lipid classes in database including 71 sub-species were chosen for identification. Adducts of +H, +NH4 were applied for positive mode search and –H, +HCO3 were selected for negative mode since ammonium bicarbonate was used in mobile phases. Only the lipids with chromatographic area >5E6 were considered as confident identification. 0.25 min retention time shift was allowed for quantitation. The protein quantification of each sample was used for normalization.

Glucose and insulin tolerance test

For glucose tolerance test (GTT), the mice were fasted for 14 hours and intraperitoneally injected with 1g/kg glucose solution. For the insulin-tolerance test (ITT), the mice were fasted for 5 h and intraperitoneally injected with 0.8 U/kg insulin solution (Beyotime, P3376). Blood samples for glucose measurement were collected from the tail vein at the indicated time points. Glucose levels were assessed using a Sinocare Glucose Monitoring Kit.

Histological analysis

For hematoxylin and eosin (H&E) or immunohistochemistry (IHC) analysis, liver and adipose tissues were dissected, fixed in 4% PFA, embedded in paraffin and sectioned (5 μm). For IHC of adipose tissue, rehydrated sections were stained following Two-Step HRP Polymer Anti-Rat IHC Detection Kit (ZSGB-BIO, PV-9004). Briefly, the slides were placed into sodium citrate buffer (pH = 6.0) and boiled for 15 min at 98°C and washed with PBS three times. Next, peroxidase was inactivated with 3% H_2O_2 for 10 min and washed with PBS three times. The samples were blocked with 3% BSA for 30 min at room temperature, then the samples were covered with the primary antibody at the indicated concentration overnight at 4°C. The next day, the slides were washed with PBS three times, and incubated with secondary antibody for 1 h at room temperature. Then the DAB Substrate Kit (ZSGB-BIO, ZLI-9017), was used for staining. Hematoxylin was used for nuclear staining for 15 s. Finally, the samples were rinsed with running water and put into the 75%, 85%, 95% and 100% ethanol for 10 s, sequentially washed with 100% ethanol for dehydration. Samples were then rinsed in xylene for 1 min twice, mounted with a coverslip and imaged. The quantification was performed using ImageJ.

For Oil Red O staining, liver tissues were dissected, fixed in 4% PFA, dehydrated in 30% sucrose, embedded in OCT and sectioned (8 μm). Then frozen liver sections were washed with PBS and rinsed with 60% isopropanol for 1 min, stained in working Oil Red O solution for 10 min, and rinsed with 60% isopropanol for 1 min. Then slides were covered with aqueous mounting gel and imaged. The quantification was performed using ImageJ.

Bone Marrow Transplantation

Bone marrow transplantation was performed as previously described[78]. Briefly, to generate irradiated chimeras, 5 weeks old *Lyz2*-Cre *TMED10*$^{fl/fl}$ recipient mice received a lethal dose of 8 Gy radiation, followed by tail vein injection of 2 x 10^6 bone marrow cells from WT (*TMED10*$^{fl/fl}$), myeloid TMED10-KO (*Lyz2*-Cre *TMED10*$^{fl/fl}$) or TMED10-Q204L knock-in (*TMED10*$^{Q204L/Q204L}$) mice. After 3 weeks of bone marrow transplantation (BMT), all mice were subjected to HFD feeding for an additional 20 weeks.

RNA sequencing and data analysis

Liver and eWAT tissues were subjected to total RNA extraction and enrichment of mRNA, and the library construction was carried out using an VAHTS® Universal V8 RNA-seq Library Prep Kit. After quality control of the library, Illumina sequencing was carried out in illumina NovaSeq X Plus 25B platform and high-quality reads were aligned via Hisat2 (v2.2.1). The expression levels of individual genes were normalized to the fragments per kilobase million (FPKM) values via HTSeq (v0.6.1). PCA (principal component analysis) were performed using Pcomp and visualized with FactoMine in R.

Differential expression analysis of bulk RNA-seq count matrices was performed using DESeq2 in R. Raw gene-level counts were first filtered to remove lowly expressed genes (row sums $\leqslant$ 10 across all samples), normalized using the median-of-ratios method, and fitted with a negative binomial generalized linear model. Wald tests were used to estimate $\log_2$ fold-changes between conditions, with shrinkage estimation applied to dispersions and effect sizes according to the DESeq2 workflow. For each pairwise comparison between experimental groups, we generated a pre-ranked gene list by ordering all expressed genes according to the DESeq2 $\log_2$ fold-change.

Gene set enrichment analysis (GSEA) was carried out on these pre-ranked lists following the original GSEA framework[79] using the GSEA implementation in the clusterProfiler package[80]. Hallmark gene sets for *Mus musculus* (category “H”) were obtained from the Molecular Signatures Database (MSigDB) via the msigdbr package[81]. Only gene sets with sizes between 5 and 500 members were retained for analysis. Nominal P values were estimated by permutation and adjusted for multiple testing using the Benjamini–Hochberg procedure; gene sets with a false discovery rate (FDR) < 0.25 were considered significantly enriched, in accordance with the original GSEA recommendations.

For gene set scoring and visualization, the inflammatory response gene set comprised *Il1b, Il1a, Il6, Il18, Tnf, Cd80, Cd68, Cd40, Ccl2, Ccl3, Ccl4, Ccl6, Cxcl2* and *Cxcl1*. The metabolic elastic gene set comprised *Angptl8, Irf4, Lep, Pnpla3, Dgat2, Thrsp, Acly, Pdk4, Fasn, Depp1, Rbp7, Thbs1, Peg3, Gm5460, Scd2, Igfals, Mycl, Ptges, Trp53inp1* and *Gpd1*. For each bulk RNA-seq sample, variance-stabilized counts obtained from DESeq2 were used as input to the

GSVA R package to compute sample-wise enrichment scores for each gene set. Heatmaps depict Z score–scaled expression values of individual genes within each set across samples. Violin plots display the distribution of gene set scores for each experimental group. Statistical comparisons of gene-set scores between groups were performed using two-sided Wilcoxon rank-sum tests.

Single-cell RNA-seq data processing and analysis

Raw FASTQ files from single-cell RNA sequencing were processed using Cell Ranger (10x Genomics) to generate gene–cell expression count matrices for each sample[82]. The resulting matrices were analyzed in R (version 4.3.2) using the Seurat package (version 4.2.1)[83,84]. Cells with fewer than 200 detected genes or more than 20% of reads mapping to mitochondrial genes were excluded, and genes detected in fewer than 3 cells were removed from the dataset. Putative doublets were identified and removed using the DoubletFinder package (version 2.0.3)[85] in combination with manual inspection of cluster-specific expression profiles. After quality control and doublet removal, cells from all dietary conditions (chow and different durations of high-fat diet feeding) were retained for downstream analysis. Publicly available human adipose tissue single-cell datasets (GSE156110)[13] and mouse adipose tissue single-cell datasets (GSE128518)[11] were processed using the same pipeline and quality-control criteria.

Gene expression counts were normalized using log-normalization with a scale factor of 10,000, and the top 2,000 highly variable genes were identified for each sample using the variance-stabilizing transformation implemented in Seurat. Datasets from different samples and experimental conditions were then integrated using the canonical correlation analysis–based integration framework to correct for batch effects[84]. Principal component analysis was performed on the integrated Seurat object, and the top 30 principal components were used for dimensionality reduction and clustering. Unsupervised clustering was carried out using a shared nearest-neighbor graph and the Louvain algorithm, and the results were visualized using Uniform Manifold Approximation and Projection (UMAP)[86].

Cell clusters were annotated to major stromal and immune cell types (B cells, NK/T cells, macrophages, dendritic cells (DCs), mast cells, neutrophils, fibro-adipogenic progenitors (FAPs), and endothelial cells) using canonical marker genes and differentially expressed genes (DEGs) identified by Seurat's FindAllMarkers function. For focused analyses of myeloid cells, macrophages were subsetted based on marker expression and reclustered.

Spatial transcriptomics dataset and label transfer

Spatial transcriptomic data of gonadal WAT from mice subjected to diet-induced obesity were obtained from publicy datasets (GSE198012)[12]. Spot–gene count matrices and the corresponding histology images were downloaded from the public repository and processed using the Seurat workflow. Low-quality spots with low total UMI counts, low numbers of detected genes or high mitochondrial transcript fractions were excluded based on the distribution of these metrics. The remaining spots were log-normalized in the same manner as the single-cell RNA-seq data.

To map ATM states onto the spatial transcriptomic data, we used our integrated mouse scRNA-seq dataset as a reference and performed anchor-based label transfer using Seurat package (FindTransferAnchors/TransferData). ATMs from the reference object were used to identify transfer anchors with spatial spots enriched for myeloid signatures, and predicted ATM cluster labels and associated module scores were obtained for each spot. Crown-like structures (CLSs) were identified on the matched H&E-stained images based on characteristic adipocyte morphology and dense macrophage aggregates, and were manually annotated by an observer blinded to the transferred cluster labels. For each ATM-labeled spot, the euclidean distance to the nearest CLS was calculated from the spot coordinates and the centroid of the annotated CLS and converted to micrometres using the array-specific scale factor. Distances were then grouped by ATM cluster to quantify the spatial enrichment of macrophage subsets.

Metabolic pathway activity analysis

For the quantification of metabolic pathway activity at single-cell resolution, we used the scMetabolism R package on the integrated Seurat objects (scMetabolism)[87]. Pathway activity scores for KEGG metabolic pathways were calculated for each cell using the sc.metabolism. Seurat function with default parameters, starting from the normalized Seurat object. This function returns the same Seurat object with an additional assay named “METABOLISM”, in which the pathway activity matrix (cells × pathways) is stored. For downstream analyses and visualization, pathway activity scores were extracted from the METABOLISM assay and summarized by group (dietary condition or ATM cluster). In the bubble plots, bubble color represents the mean normalized pathway activity for a given pathway within each group, and bubble size indicates the proportion of cells in that group with non-zero activity.

Inflammatory-response gene-set scoring

For the quantification of inflammatory activity at the single-cell resolution, we constructed an inflammatory-response gene set based on KEGG pathway annotations HALLMARK_INFLAMMATORY_RESPONSE)[81,88], and the full gene list is provided in

Supplementary Table 6). Differentially expressed genes among ATM clusters were first identified using Seurat's FindMarkers/FindAllMarkers functions, and KEGG pathway enrichment analysis was performed using the KEGG database[89]. Per-cell enrichment scores for the inflammatory gene set were then calculated using the AddModuleScore function in Seurat, which summarizes the relative expression of genes in the module compared with control genes of matched expression levels.

Gene set variation analysis (GSVA) / single-sample GSEA

For the evaluation of coordinated changes in metabolic and inflammatory pathways across ATM clusters, we performed single-sample gene set enrichment analysis using the GSVA R/Bioconductor package[90]. Log-normalized expression values from the integrated Seurat object were used as input for the gsva function (method = "ssgsea"), thereby computing an enrichment score for each gene set in each cell. Gene sets were curated mainly from the MSigDB Hallmark collection, including fatty acid metabolism, cholesterol homeostasis, oxidative phosphorylation, glycolysis, IFNα response, IFNγ response, IL2–STAT5 signaling, TNFα signaling via NFκB, lipid transport, and lipid metabolic process terms[79,81]. For visualization, single-cell enrichment scores were normalized within ATM clusters to obtain cluster-level enrichment scores, and then displayed using heatmaps in which color represents the mean enrichment score per pathway and cluster.

Plasmids and shRNA oligos

The TMED10, mIL-1β expression and purification plasmids were described previously[29]. The TMED10 mutations were generated by mutagenesis PCR. SGMS1 and SMPD2 were PCR amplified from cDNA and inserted into FUGW vectors with a HA tag at the C-terminus for mammalian cell expression. Sphingomyelinase was PCR amplified from the *Staphylococcus aureus* genome which was a gift from Dr. Jing-Ren Zhang (Tsinghua University) and was inserted into the pET28a vector. pET28a-Eqt-SM was a gift from Dr. Yong-Qiang Deng (Southern Medical University).

For shRNAs, the plasmids (pLKO.1 lentivirus vector as a backbone) were purchased from the Center of Biomedical Analysis, Tsinghua University. The targeting sequences of these shRNAs were shown in the **Extended Data Table 2.**

Transfection and lentiviral transduction

Transfection of plasmids into cells was performed using polyethylenimine (PEI) (Polysciences, Inc.) for HEK293T and NEOFECT (Neofect (Beijing) biotech Co. Ltd.) or X-tremeGENE HP (Roche) or Sage LipoPlus (Sage (Beijing) Chemical Co. Ltd.) for U2OS and HeLa according to the manufacture's protocols. For lentiviral transduction, pLKO.1 plasmids carrying Control,

SMPD2, SGMS1, SGMS2 or CERT target sequence was transfected into HEK293T cells along with lentiviral packaging plasmids pMD2.G and psPAX2 (Addgene) using PEI to produce lentiviral particles to infect HEK293T cells.

Preparation of PA-BSA and SM-BSA complexes

For PA-BSA complex preparation, fatty-acid-free BSA (yeasen, 36104ES25) was dissolved in PBS to 200 mg/ml. 20 mM palmitic acid (PA, sigma, P0500) was dissolved and saponified in 0.1 M NaOH at 70°C, and then mixed with an equal volume of BSA solution at 55°C with shaking for 1 h to allow for complex formation. The final PA-BSA solution is clear and the molar ratio of PA:BSA is approximately 6:1. For the preparation of SM-BSA complex[91], fatty-acid-free BSA was dissolved in PBS to 1 mM. A solution of 10 mg/ml of SM (the molar ratio of SM to BSA was 1:1) in absolute ethanol was added in small aliquots to a stirred solution of 1 mM BSA at 37°C until a clear solution was achieved. The PA-BSA and SM-BSA complexes were filtered through 0.22 μm syringe filters (Pall Corporation) and replenished in culture medium at the indicated concentration and time durations, with an equal concentration of BSA solution as vehicle control.

Secretion and serum lipid determination

For determination of mIL-1β secretion in HEK293T cells[29], cell culture medium was replaced with DMEM containing indicated drugs for 1.5 hours. The medium was collected and concentrated (20-fold) by a 10 kDa Amicon filter (Millipore). Cells were lysed in SDS-PAGE loading buffer. Immunoblot was performed to determine the amounts of cargoes in the medium and cell lysate.

The IL-1β secretion in THP-1 cells, peritoneal macrophages or mice plasma were detected using the ELISA kit. For the detection of IL-1β secretion in WT and TMED10-KO THP-1 cells, THP-1 cells were first differentiated by incubation with 50 nM PMA for 20 h, and then treated with 50-150 μM PA-BSA and 5 μM MCC950, 9 μM Ac-YVAD-cmk, 10 μM Mal C or 10 μM Eliglustat in complete medium for 16 h. For the detection of IL-1β secretion in peritoneal macrophages, cells were induced with 100 ng/ml LPS in RPMI-1640 plus 10% FBS followed by 5 μM Nigericin or 2 mM ATP treatment for 60 min in complete medium. Alternatively, the peritoneal macrophages were treated with PA-BSA and other drugs at indicated concentration and time durations. The medium from THP-1 cells or peritoneal macrophages were collected for IL-1β concentration determination using ELISA kit.

Plasma glycerol (APPLYGEN, E1002-125), plasma NEFA (Nanjing Jiancheng, A042-2-1) and hepatic triglyceride (Nanjing Jiancheng, A110-1-1) were measured according to the manufacturer's instructions.

Immunofluorescence

Immunofluorescence was described previously[29]. Briefly, cells were washed twice with PBS and then fixed with 4% paraformaldehyde at room temperature for 20 min (for general staining) or cold methanol at -20°C for 8 min (for endogenous TMED10 and ERGIC53 staining). The cells were washed twice with PBS and permeabilized with 0.2% Triton X-100 diluted in PBS for 3 min. After washing with PBS three times, cells were blocked by 10% FBS diluted in PBS at room temperature for 1 h and followed by primary antibody incubation at room temperature for 2 h or 4°C overnight. Cells were washed with PBS three times and followed by secondary antibody incubation at room temperature for 1 h. Fluorescence images were acquired at room temperature using the Olympus FV3000 laser scanning confocal microscope equipped with a 1.3 NA 60× oil-immersion objective and FV31S acquisition software.

In situ Duolink

Duolink PLA kit was purchased from sigma (DUO92002, DUO92004, DUO92014) and the assay was performed according to the product manual. For self-interactions of TMED10 detection, equal amounts of TMED10-V5 and TMED10-3*FLAG were co-expressed without or with SGMS1-HA or SMPD2-HA in U2OS cells. After 24 h transfection, the cells were washed twice with PBS and then incubated with 4% cold paraformaldehyde at room temperature for 20 min. The cells were washed twice with PBS and permeabilized with 0.2% Triton X-100 diluted in PBS for 3 min. The cells were blocked, incubated with primary antibodies and PLA probes followed by ligation and amplification using the recommended conditions according to the manual. The anti-rat secondary antibodies (for HA tag staining) were added during the ligation step. Images were acquired using the Nikon AX confocal microscope and quantification was performed using ImageJ.

Protein expression and purification

For the expression of GST-tagged TMED10, his-tagged T7-mIL-1β-FLAG, mIL-1RA, sphingomyelinase, Eqt-SM, the constructs were transformed into the *E.coli* strain BL21 (DE3) plysS. After transformation, a single colony was picked and grown in 600 μL LB medium at 37°C with shaking at 220 rpm for approximately 6 hours. The pre-culture was further expanded to 50 mL and incubated overnight under the same conditions. The next day this culture was scaled up to 1 L LB medium followed by incubating at 37°C with shaking at 220 rpm until the OD_{600} reached 0.6-0.8. A final 100 μM IPTG was added to the culture and the protein expression was induced at 16°C with shaking at 160 rpm overnight. After expression, the bacterial pellets were collected and stored at -80°C for subsequent purification.

For the expression of FLAG-tagged TMED10, the protein was expressed in HEK293F suspension cells (from Dr. Shan Sun and Dr. Sen-Fang Sui). The encoding DNA of TMED10 was cloned into a vector pCMV-3*FLAG containing an N-terminal 3*FLAG tag after the signal

sequence. When the density of HEK293F cells reached 2.0 × 10^6 cells/ mL, the cells were transfected with the expression plasmids using PEI. 1.5 mg of plasmids and 3 mg of PEI, each in 25 mL of fresh medium, were premixed for 30 min, and then 50 mL of the mixture was added to 800 mL of cell cultures. The transfected cells were grown for 48 hours and then harvested.

For purification of GST-tagged TMED10, cell pellets were lysed in lysis buffer (50 mM Tris 8.0, 5 mM EDTA,150 mM NaCl,10% glycerol, 0.5 mg/mL lysozyme, 0.3 mM DTT and 1 mM PMSF) and then rotated at 4°C for 0.5 h. Triton X-100 was added to achieve 1% final concentration and incubated for an additional 10 minutes. The lysates were sonicated and then centrifuged at 20,000 rpm for 1 h. The supernatant was collected and incubated with 0.5 mL of Glutathione Sepharose 4FF beads at 4°C for 2 h. After incubation, the beads were washed with 15 bed volumes of wash buffer (PBS with 0.1% Triton X-100). The proteins were eluted with elution buffer (50 mM Tris 8.0, 250 mM KCl, 25 mM glutathione, and 0.1% Triton X-100), concentrated by Amicon® Ultra Filters (Merck) and further purified by size-exclusion chromatography (SEC) on a Superose 6 increase column (Cytiva) in SEC buffer (PBS with 0.1% TritonX-100). The proteins were snap-frozen by liquid nitrogen and stored at -80°C.

For purification of his-tagged mIL-1RA, mIL-1β, Eqt-SM and sphingomyelinase, cell pellets were lysed in lysis buffer (2 x PBS, 10 mM imidazole, 0.5 mg/mL lysozyme, 0.3 mM DTT and 1 mM PMSF) and then rotated at 4°C for 0.5 h. The lysates were sonicated and centrifuged at 20,000 rpm for 1 h. The supernatant was incubated with 0.5 mL Ni-NTA agarose at 4°C for 2 h. The agarose was washed with 10 bed volumes of wash buffer containing 0.1% Tween20 and wash buffer (2 x PBS, 25 mM imidazole) followed. The proteins were eluted with elution buffer (2 x PBS, 250 mM imidazole). The proteins were concentrated by Amicon® Ultra Filters (Merck) and desalted by PD MiniTrap G-25 (Cytiva). For his-tagged mIL-1RA and his-tagged mIL-1β, the endotoxin was removed by incubating purified proteins with endotoxin removal resin (Thermo, Cat#88274) overnight at 4°C. The proteins were snap-frozen by liquid nitrogen and stored at -80°C. To test biological activity, HEK-Blue™ IL-1β cells (InvivoGen) were treated with 5 μg/ml his-tagged mIL-1RA, 0.1 μg/ml his-tagged mIL-1β, or both, and SEAP activity in medium was detected using QUANTI-Blue™ Solution (InvivoGen, rep-qbs).

For purification of FLAG-tagged TMED10, collected cells were solubilized in lysis buffer (20 mM HEPES (pH = 7.4), 150 mM NaCl, 1% DDM, and 1 mM PMSF) at 4°C for 1 h. After centrifugation at 35,000 rpm at 4°C for 1 h, the supernatant was collected and incubated with FLAG affinity resin (Sigma-Aldrich) at 4°C for 1 h. Then the resin was washed with 15 bed volumes of wash buffer (20 mM HEPES (pH = 7.4), 150 mM NaCl, 0.02% DDM). The protein was eluted using elution buffer (20 mM HEPES (pH = 7.4), 150 mM NaCl, 0.02% DDM, and 0.1 mg/mL 3×FLAG peptide). The eluted proteins were concentrated using Amicon® Ultra Filters (Merck) and further purified by size-exclusion chromatography (SEC) on a Superose 6 Increase

Column (Cytiva) in SEC buffer (20 mM HEPES (pH = 7.4), 150 mM NaCl, 0.02% DDM). Finally, the proteins were snap-frozen by liquid nitrogen and stored at -80°C.

Lipid preparation for proteoliposome reconstitution

DOPC (1,2-dioleoyl-sn-glycero-3-phosphocholine, Cat# 850375P), DOPE (1,2-dioleoyl-sn-glycero-3-phosphoethanolamine, Cat# 850725P), Liver PI (L-α-phosphatidylinositol, Cat# 840042P), Lyso PC (1-oleoyl-2-hydroxy-sn-glycero-3-phosphocholine, Cat# 840072P), Brain SM (Brain, Porcine, Cat# 860062P), Cholesterol (ovine, Cat# 700000P), Ceramide (Brain, Porcine, Cat# 860052P), Cardiolipin (1',3'-bis[1,2-dioleoyl-sn-glycero-3-phospho]-glycerol (sodium salt), Cat# 710335P), 18:0 CPE (Ceramide phosphoethanolamine, Cat# 860066P), 16:0 SM (d18:1/16:0, Cat# 860584P), 18:0 SM (d18:1/18:0, Cat# 860586P), 24:1 SM (d18:1/24:1, Cat# 860593P)-d9 were purchased from Avanti Polar Lipids. 20:0 SM (d18:1/20:0, Cat# 24450) and 22:0 SM (d18:1/22:0, Cat# 24451) were purchased from Cayman Chemical.

Lipids were initially dissolved in chloroform at specific concentration. Then, the lipids were mixed with specific molar concentration as indicated. The mixtures were dried with a nitrogen stream and further dried at 37°C for 1 h. The lipid films were hydrated in HEPES-KAc buffer (20 mM HEPES (pH 7.2), 150 mM potassium acetate) and incubated at 220 rpm at 37°C for 1 h to resuspend thoroughly. The hydrated lipids could be aliquoted and stored at -80°C for further use.

In vitro translocation and protease K protection assay

Proteoliposome reconstitution was performed according to a previous study with minor modifications[29]. 1 mg lipids for each reaction tube were frozen in liquid nitrogen and thawed in a 42°C water bath alternately for 10 times. Triton X-100 was added to achieve a final concentration of 0.05%, and the mixture was rotated at 4°C for approximately 30 minutes. Next, 10 μg recombinant proteins (GST-TMED10) were added to the lipid solution (10 μg recombinant proteins, 1 mg lipids, and 0.05% Triton X-100 in 400 μL solution) and the mixture was rotated at 4°C for 1 h. Each solution was incubated with 6-8 mg Bio-Beads SM2 Resin (Bio-Rad) which was pre-equilibrium by HEPES-KAc reaction buffer to remove the detergent and rotated at 4°C for approximately 1 h. This step was repeated 5 times (10 mg beads used during the third incubation, which was extended overnight). The Bio-Beads were removed by 1,500 × *g* centrifugation at 4°C each step and after the last time, the liposome solution were froze in liquid nitrogen and thawed in a 42°C water bath alternately for 5 times. To remove the free proteins, a membrane flotation step was performed. For each 350 μL solution, 350 μL 50% OptiPrep (diluted in HEPES-KAc buffer) was added. The mixture was overlaid with 560 μL 20% OptiPrep and 105 μL HEPES-KAc buffer, centrifuged at 100,000 × *g* for 2 h and the top 200 μL fraction was collected and diluted with 100 μL HEPES-KAc buffer as proteoliposome solution.

For the in vitro protein translocation, 10 μg cargo proteins (T7-mIL-1β-FLAG) were pretreated with 4 M urea for at least 30 min and diluted into proteoliposome solution (150 μL system) and then incubated at 30°C for 1 h. After incubation, 5 μL reaction buffer was taken as input and the left was added 150 μL 50% OptiPrep (diluted in HEPES-KAc buffer). The mixture was overlaid with 240 μL 20% OptiPrep and 45 μL HEPES-KAc buffer, centrifuged at 45,000 rpm for 2 h and the 90 μL top fraction was collected and aliquoted into 3 fractions. All fractions were loaded to 50 μL. The first fraction was a control, the second and the third fractions were digested by 10 μg/ml protease K without or with 0.1% Triton X-100 for 20 min on ice. The reactions were stopped by 1 mM PMSF and incubated for 10 min on ice. Finally, 2 × SDS loading buffer was added and the samples were heated at 100°C for 10 min followed by immunoblot analysis.

Analysis of gene expression level

Gene expression was determined by qRT-PCR. Total RNA was isolated using Trizol (Beyotime) and cDNA was generated using ABScript III RT Master Mix for qPCR (ABclonal) according to the manufacturer's protocols. The samples were amplified using a CFX-96 machine (Bio-Rad) and SYBR Green T5 Fast qPCR mix (TSINGKE, China) according to the manufacturer's instructions. Data were normalized to the Actin control. The sequences of the primers were listed in the **Extended Data Table 3**.

Lipid extraction and dot blot of sphingomyelin

Total cell lipids were extracted as previously reported[29]. Detailly, cells were collected and washed with PBS. After centrifugation at 600 × *g* for 5 min, the cell pellets were resuspended in PBS (cell pellets: PBS =1: 1). Then, chloroform/methanol solution was added to the cell suspension (chloroform: methanol: cell suspension = 8: 4: 3) and vortexed for 30 s. The mixtures were shaken for 0.5 h at 37°C. The chloroform phase was collected and evaporated by a stream of nitrogen gas over the lipid solution and further dried at room temperature for 0.5 h. Dried lipid was dissolved in ethanol. The phosphatidylcholine content of the lipid solution was measured by a standard kit (Wako) to normalize lipid concentration. Equal amounts of lipids were spotted on the nitrocellulose membrane and dried at room temperature for 0.5 h. The blot was first blocked for 2 h in 4% (w/v) fatty-acid-free bovine serum albumin (BSA) dissolved in TBS (20 mM Tris-HCl, 150 mM NaCl, pH 7.6), and then incubated with Flag-tagged equinatoxin II (Eqt-SM)[92] at final 2.5 μg/ml concentration, anti-Flag primary antibodies and secondary antibodies conjugated with horseradish peroxidase for 2 h in 4% BSA dissolved in TBST (TBS-0.1% Tween-20). The membrane was finally washed with TBST for three times (each times for 10 min).

Crosslink assay

DSS was dissolved in DMSO before use. The in vivo DSS crosslink assay was described previously[29]. Peritoneal macrophages and adipose tissue macrophages were isolated as described above. The macrophages or TMED10-KO HEK293T cells were washed with PBS (pH = 8.0) three times and then suspended in PBS (pH = 8.0) with the indicated concentration of DSS at room temperature for 30 min. Then the reactions were quenched by 20 mM Tris (pH = 7.5) at room temperature for 15 min followed by sample preparation for immunoblot analysis. For in vitro DSS crosslink assay, the lipid mixtures were generated with PC, or PC supplemented with 10% SM which was treated with or without 0.5 μM sphingomyelinase when recombinant protein added. The indicated concentration of DSS was added to the proteoliposomes and the following steps were done as stated above.

Biotin sphingomyelin pulldown

Biotin sphingomyelin pulldown was performed according to a previous report with minor modifications[93]. 5 μg recombinant proteins and 2 μM biotin sphingomyelin (Echelon, S-400B) was incubated in pulldown buffer (50 mM Tris 7.4, 1 mM EDTA,150 mM NaCl, 0.2% Triton X-100, 1 mM PMSF) and rotated at 4°C for 2 h. Streptavidin sepharose beads (Cytiva, 17511301) were blocked with 10% FBS diluted in pulldown buffer for 1 h and then the beads were added to the pulldown system and further rotated at 4°C for 3 h. The samples were centrifuged at 1,000 × *g* for 1 min at 4°C, and the beads pellets were washed four times with pulldown buffer. After washing, the pellets were treated with SDS loading buffer followed by immunoblot analysis.

All-atom molecular dynamics (MD) simulations

The structure of TMED10-TMD with adjacent sequences of luminal and cytosolic regions (sequence: RDTNESTNTRVLYFSIFSMFCLIGLATWQVFYLRRFFKAKK, TMD is underlined) was truncated from full-length TMED10 in AlphaFold protein structure database[94]. In order to study the interactions between TMED10-TMD and sphingomyelin, we set up the system where TMED10-TMD was inserted in the lipid bilayer with 90% POPC (1-palmitoyl-2-oleoyl-sn-glycero-3-phosphocholine) and 10% SSM (stearoyl sphingomyelin) solvated in water with 0.15M NaCl. For the MD simulation, the CHARMM36m all-atom force field[95] and GROMACS software[96] (version 2019.4) were used to run for 100 ns with the time step of 2 fs. Nose-Hoover heat bath[97,98] of 310 K (coupling constant τ = 1 ps) and semi-isotropic Parrinello-Rahman pressure bath[99] of 1 bar (coupling constant τ = 5 ps and compressibility = 4.5×10^{-5} $bars^{-1}$ for all dimensions). All system snapshots and movies were rendered by VMD[100]. The contacts between TMED10-TMD and SM was calculated using GROMACS tool *gmx mindist*[96].

Quantification and statistical analysis

For the quantification of cargoes secretion, the relative level of cargoes in medium were normalized to cargoes and TMED10 expression level in corresponding cell lysate. For the quantification of in vitro translocation, the relative cargoes translocation efficiency were normalized to TMED10 level on proteoliposomes. For the quantification of homo-oligomer ratio in the crosslink assay, the level of homo-oligomers were normalized to the level of corresponding monomer. The immunoblotting images were acquired using ChemiDoc Imaging System (Bio-Rad). The analysis and quantification of bands were performed using Image Lab and ImageJ software. The statistical information of each experiment, including the statistical methods, the P-values, and numbers (n), were shown in the figures and corresponding legends. Statistical analyses were performed using GraphPad Prism.

Data availability

All data are available in the paper or the supplementary materials. Further information and requests for reagents should be directed to Lead Contact, Liang Ge (liangge@mail.tsinghua.edu.cn). Plasmids and cell lines generated in this study will be made available upon request. We may require a payment and/or a completed Materials Transfer Agreement in case there is potential for commercial application. Source data are provided with this paper.

Code availability

All code reported in this manuscript are available on request.

Extended Data Table 1. List of genotyping primers used in this study.

Gene	Sequence
Lyz2-Cre(F)	GCTGCCAGAATTTCTCTCATCAC
Lyz2-Cre(R)	ACATGTCCATCAGGTTCTTGCG
Lyz2-CreWT(F)	GAAGCCATTATTTCACAGCAGCA
Lyz2-CreWT(R)	CTGTCCCTGTTCTGAGCGATT
Tmed10 flox(F)	TGTCAGGAAGCGACTCCTTTT
Tmed10 flox(R)	CCAGCTTAAAGGGGATCTCAG
Gsdmd flox(F)	TTCCCTCCAGCCCTACTTGC
Gsdmd flox(R)	TGAGCATCCTTCCCAACCTG
Tmed10-Q204L(F)	AGACCTATGGACAGAATGAGGCTAAC
Tmed10-Q204L(R)	AAGGACTTCAAGCAGTTGAGCACA

Extended Data Table 2. List of shRNAs used in this study.

shRNA	Target sequences
Control shRNA	CGTGATCTTCACCGACAAGAT
SGMS1 shRNA-1	GCGTTGGACAACAATAAAGAA
SGMS1 shRNA-2	GCGAAGAATAATGAAGCTCAT
SGMS1 shRNA-3	CCTCAGTAGGCAAGTTAAATA
SGMS2 shRNA-1	GCTGTAACCAAAGGTATAGTT
SGMS2 shRNA-2	CCAGTGATCCTACGAACACTT
CERT shRNA-1	GCAAAGCGAGAGTATCCTAAA
CERT shRNA-2	GCAACACTTTCTCATTGTATT
SMPD2 shRNA-1	CGACAGAAGGACATCTACCTA
SMPD2 shRNA-2	CAGGAGGTCAATGGCTTATAT

Extended Data Table 3. List of qPCR primers used in this study.

Gene	Sequence
Actin(F)	CATGTACGTTGCTATCCAGGC
Actin(R)	CTCCTTAATGTCACGCACGAT
SGMS1(F)	TGTGCCGAGTCTCCTCTGA
SGMS1(R)	CCGTTCTTGTGTGCTTCCAAA
SGMS2(F)	TCCTACGAACACTTATGCAAGAC
SGMS2(R)	CCGGGTACTTTTTGGTGCCT
CERT(F)	AAAGGCCACAGTTTACGTGAG
CERT(R)	CTTCTGTAGCGTGTCAACTTGT
SMPD2(F)	TCAATGGCTACCCCTACATGA
SMPD2(R)	ATGCCACTTAGATGGAGCACC

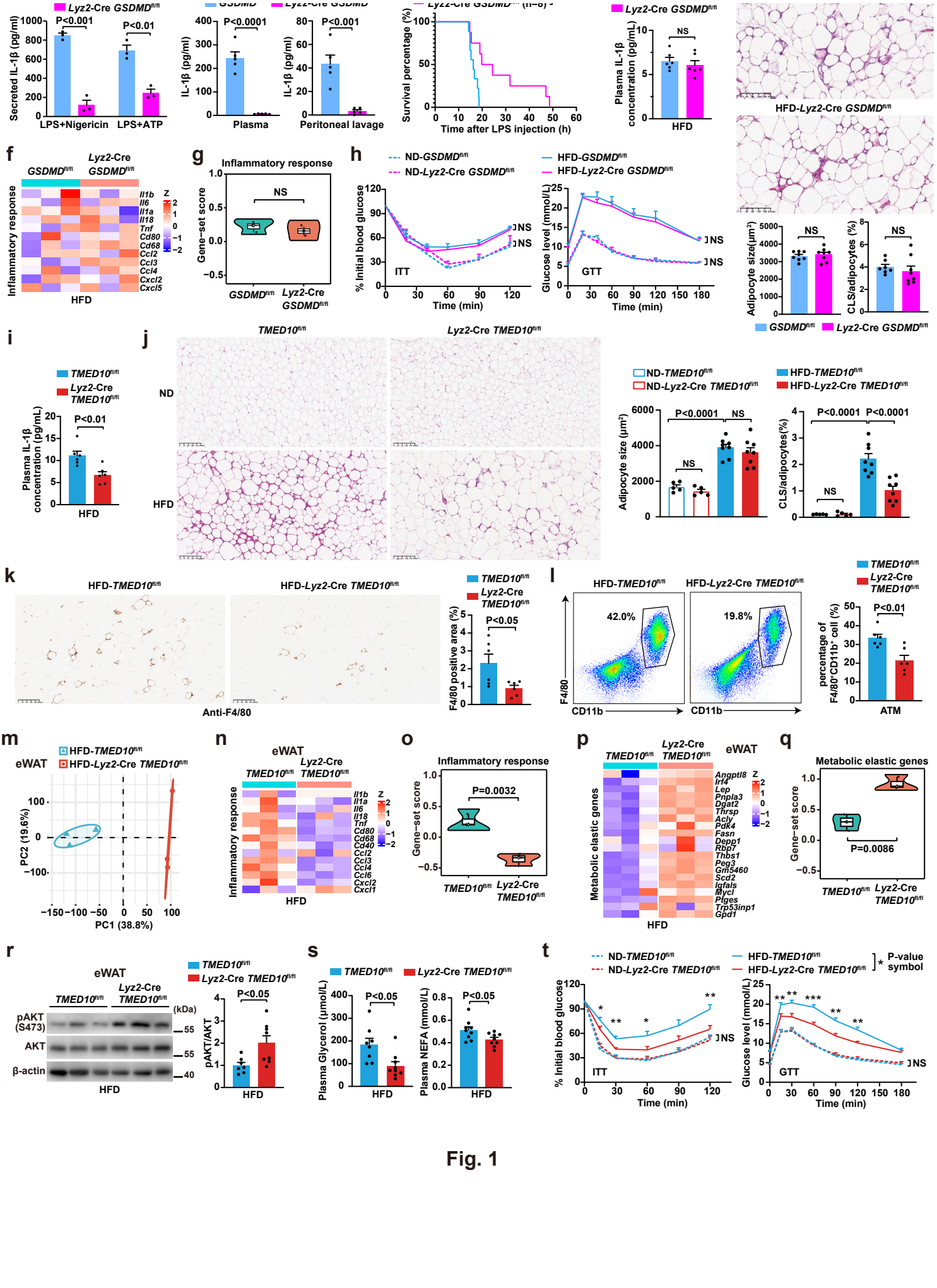

Fig. 1

Fig. 1 | TMED10, but not GSDMD, mediates HFD-induced metabolic inflammation and dysfunction. **a**, ELISA analysis of IL-1β secretion in LPS-primed (50 ng/mL) peritoneal macrophages following treatment with Nigericin (5 μM, 1 h) or ATP (2 mM, 1 h). **b**, IL-1β in plasma and peritoneal lavage measured by ELISA 12 h after LPS challenge (25 mg/kg, male) (n=5). **c**, Survival curves after LPS challenge (n=8). **d**, *GSDMD*$^{fl/fl}$ mice and *Lyz2*-cre *GSDMD*$^{fl/fl}$ mice (male) were fed on ND or HFD for 12 weeks. Plasma IL-1β was determined by ELISA (n=6). **e**, H&E staining of eWAT for quantification of adipocyte size and crown-like structure (CLS) percentage (n=8). **f**, Heatmap analysis of genes involved in inflammatory response in eWAT. **g**, gene-set score of (**f**). **h**, GTT(n=7-9) and ITT (n=6-8) in mice of ND or HFD**. i**, *TMED10*$^{fl/fl}$ mice and *Lyz2*-cre *TMED10*$^{fl/fl}$ mice (male) were fed on ND or HFD for 12 weeks. Plasma IL-1β was determined by ELISA (n=6). **j**, H&E staining of eWAT for quantification of adipocyte size and crown-like structure (CLS) percentage (n=5-8). **k**, IHC for F4/80^{+} macrophages in eWAT (n=6). **l**, Flow cytometric analysis of F4/80^{+} CD11b^{+} macrophages in eWAT (ATM). **m**, PCA of eWAT from RNA-seq. **n**-**q**, Heatmap analysis of genes involved in inflammatory response (**n**) or metabolic elastic genes (**p**) with corresponding gene-set score in eWAT (**o, q**). **r**, Western blot analysis of pAKT (S473) and quantification in eWAT after insulin administration for 15 min (n=7-8). **s**, Plasma glycerol and NEFA levels in mice fasting for 16 h (n=8-9). **t**, GTT (n=7-8) and ITT (n=6-7) in mice of ND or HFD**.** NS, non-significant; *P < 0.05; **P < 0.01; ***P < 0.001; ****P < 0.0001. All values are presented as mean ± s.e.m. P values were calculated by unpaired two-tailed Student's t-test (**a, b, d, e, i, k, l, r, s**), two-sided Wilcoxon rank-sum test (**g, o, q**), one-way ANOVA followed by Tukey's test (**h, j, t**) or log-rank (Mantel–Cox) test (**c**).

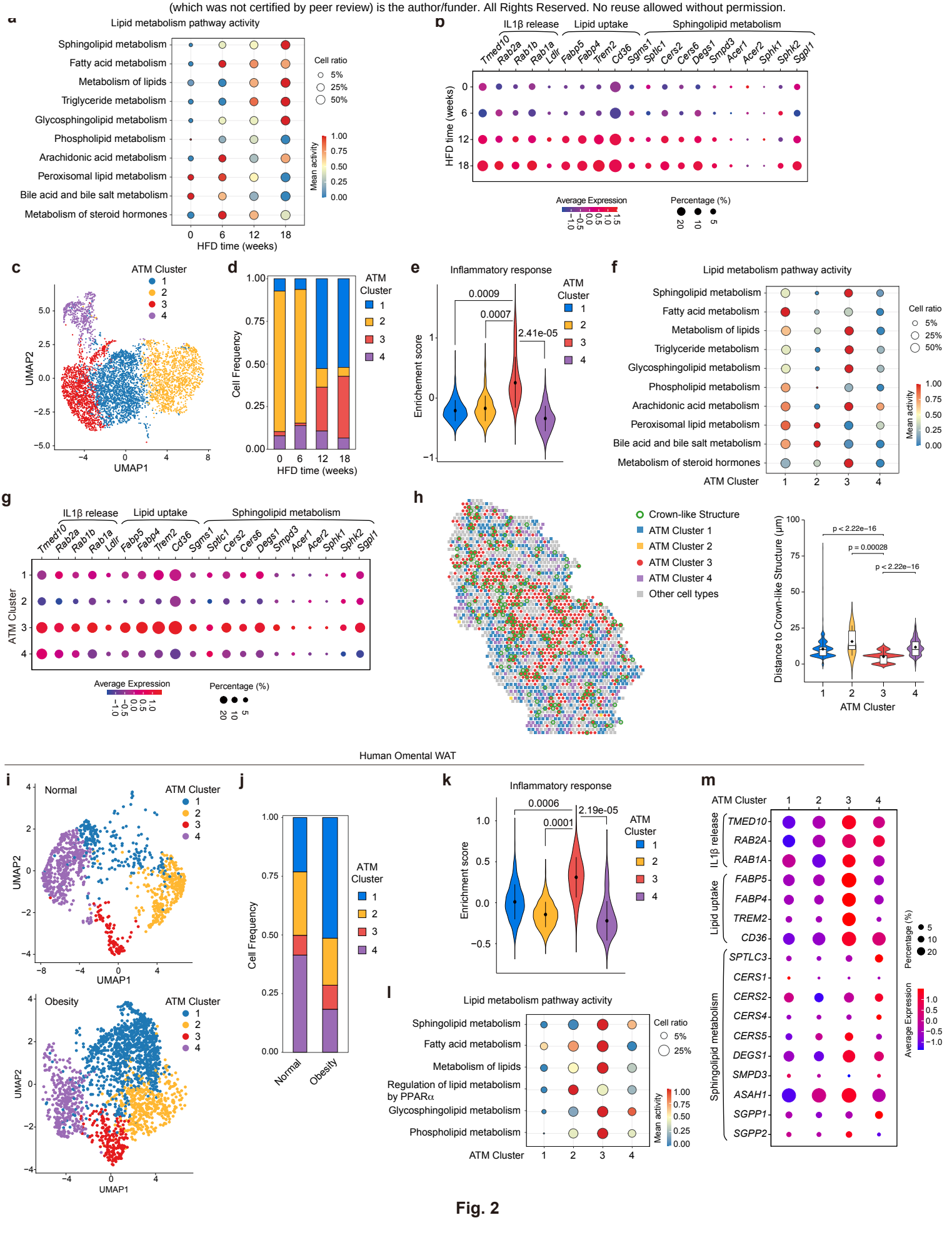

Fig. 2

Fig. 2 | TMED10 couples sphingomyelin metabolism to the emergence of metabolically inflammatory macrophages in obese adipose tissue. a, Bubble plot showing lipid metabolism pathway activity in eWAT adipose tissue macrophages (ATMs) from mice fed chow (0 weeks) or a high-fat diet (HFD) for 6, 12, or 18 weeks. Circle size indicates the proportion of cells with pathway activity, and color indicates mean pathway activity. **b,** Dot plot depicting expression of gene modules associated with IL-1β release, lipid uptake, and sphingomyelin metabolism in eWAT ATMs at the indicated HFD durations. Dot size represents the fraction of expressing cells, and color indicates scaled average expression. **c,** UMAP visualization of mouse eWAT ATMs, colored by four transcriptionally defined clusters (ATM clusters 1–4). **d,** Bar graph showing relative frequency of each ATM cluster among total ATMs over the course of HFD feeding. **e,** Violin plots of an inflammatory-response gene-signature score in ATM clusters 1–4. **f,** Bubble plot showing lipid metabolism pathway activity in each ATM cluster; circle size indicates the proportion of cells with pathway activity, and color indicates mean pathway activity. **g,** Dot plot depicting expression of gene modules associated with IL-1β release, lipid uptake, and sphingomyelin metabolism in ATM clusters 1–4. Dot size represents the fraction of expressing cells, and color indicates scaled average expression. **h,** Spatial transcriptomics of eWAT from long-term HFD-fed mice showing the spatial distribution of ATM clusters relative to crown-like structures (CLSs; left), and violin plots quantifying the distance from each ATM to the nearest CLS (right). **i,** UMAP plots of human adipose tissue macrophages from metabolically normal and obese individuals, colored by four transcriptionally defined clusters (ATM clusters 1–4). **j,** Bar graph showing relative frequency of human ATM clusters in normal versus obese visceral adipose tissue. **k,** Violin plots of inflammatory-response gene-set scores in human ATM clusters 1–4. **l,** Bubble plot showing lipid metabolism pathway activity in each human ATM cluster; circle size indicates the proportion of cells with pathway activity, and color indicates mean pathway activity. **m,** Dot plot depicting expression of gene modules associated with IL-1β release, lipid uptake, and sphingomyelin metabolism in human ATM clusters. Dot size represents the fraction of expressing cells, and color indicates scaled average expression. Statistical tests were performed using two-sided Wilcoxon rank-sum tests (**e, h, k**).

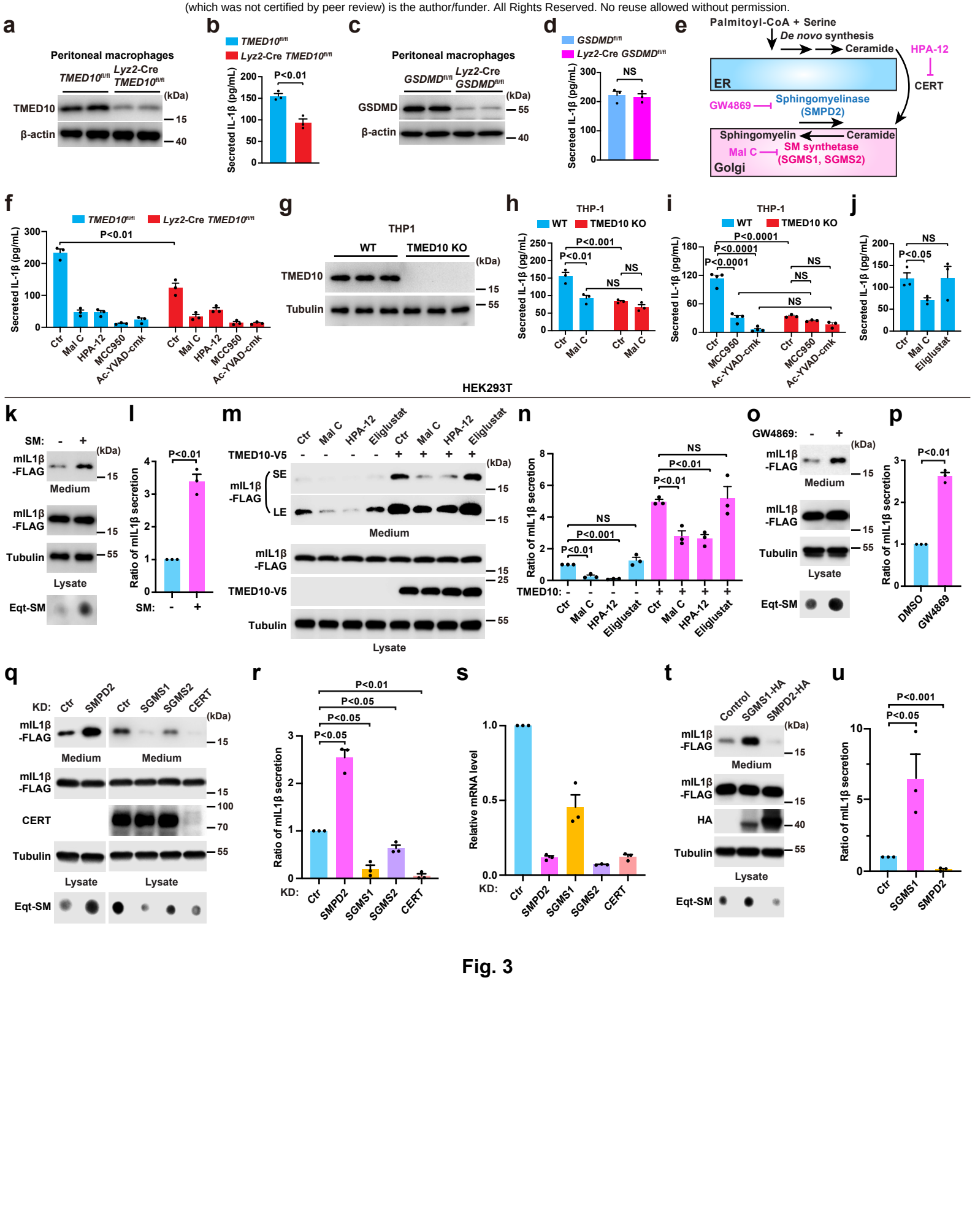

Fig. 3

Fig. 3 | Sphingomyelin enhances TMED10-mediated IL-1β secretion. a, The TMED10 protein level in macrophages from *TMED10*$^{fl/fl}$ and *Lyz2*-cre *TMED10*$^{fl/fl}$ mice. **b,** ELISA analysis of IL-1β secretion following 150 μM PA stimulation for 24 h in peritoneal macrophages of *TMED10*$^{fl/fl}$ and *Lyz2*-cre *TMED10*$^{fl/fl}$ mice mice. **c,** The GSDMD protein level in macrophages from *GSDMD*$^{fl/fl}$ and *Lyz2*-cre *GSDMD*$^{fl/fl}$ mice. **d,** ELISA analysis of IL-1β secretion following 150 μM PA stimulation for 24 h in peritoneal macrophages of *GSDMD*$^{fl/fl}$ and *Lyz2*-cre *GSDMD*$^{fl/fl}$ mice. **e,** Schematic diagram of the sphingomyelin metabolism pathway with inhibitors of key processes labeled. **f,** ELISA analysis of IL-1β secretion following 150 μM PA stimulation for 24 h in peritoneal macrophages of *TMED10*$^{fl/fl}$ and *Lyz2*-cre *TMED10*$^{fl/fl}$ mice. The macrophages were treated without or with 10 μM Malabaricone C (Mal C), 20 μM HPA-12, 5 μM MCC950 or 10 μg/ml Ac-YVAD-cmk for 24 h. **g,** The TMED10 protein level in WT and TMED10 KO THP-1 cells. **h,** ELISA analysis of IL-1β secretion following 50 μM PA stimulation for 16 h in WT or TMED10 KO THP-1 cells treated without or with 10 μM Mal C. **i,** ELISA analysis of IL-1β secretion following 50 μM PA stimulation for 16 h in WT or TMED10 KO THP-1 cells treated without or with 5 μM MCC950 or 9 μM Ac-YVAD-cmk. **j,** ELISA analysis of IL-1β secretion following 150 μM PA stimulation for 16 h in WT THP-1 cells treated without or with 10 μM Mal C or 10 μM Eliglustat. **k,** Secretion of mIL-1β in HEK293T cells treated with 20 μM BSA (control) or 20 μM BSA-SM complex for 16 h. SM in these cells was determined by the SM probe Eqt-SM using a dot blot assay (bottom). **l,** Quantification of mIL-1β secretion from (**k**) (n = 3). **m,** Secretion of mIL-1β in HEK293T cells without or with TMED10-V5 expression. The cells were treated without or with 10 μM Malabaricone C (Mal C), 5 μM HPA-12 or 10 μM Eliglustat for 16 h. **n,** Quantification of mIL-1β secretion from (**m**) (n = 3). **o,** Secretion of mIL-1β in HEK293T cells treated without or with 5 μM GW4869 for 16 h. SM was determined by Eqt-SM (bottom). **p,** Quantification of mIL-1β secretion from (**o**) (n = 3). **q,** HEK293T cells with mIL-1β expression were infected by lentiviral particles packaged with indicated shRNA vectors. 96 hours post infection, mIL-1β secretion was analyzed. SM was determined by Eqt-SM (bottom). **r,** Quantification of secretion from (**q**) (n = 3). **s,** QPCR analysis of gene knockdown efficiency from (**q**) (n = 3). **t,** Secretion of mIL-1β in HEK293T with control, SGMS1 or SMPD2 expression to modulate the cellular SM level. SM was determined by Eqt-SM (bottom). **u,** Quantification of secretion from (**t**) (n = 3). All values are plotted as mean ± s.e.m. P values were calculated by two-tailed Student's t-test (**b, d, f, j, l, p, u**), one-way RM-ANOVA with Fisher's test (**n, r)** or two-way ANOVA with Tukey's test (**h, i**).

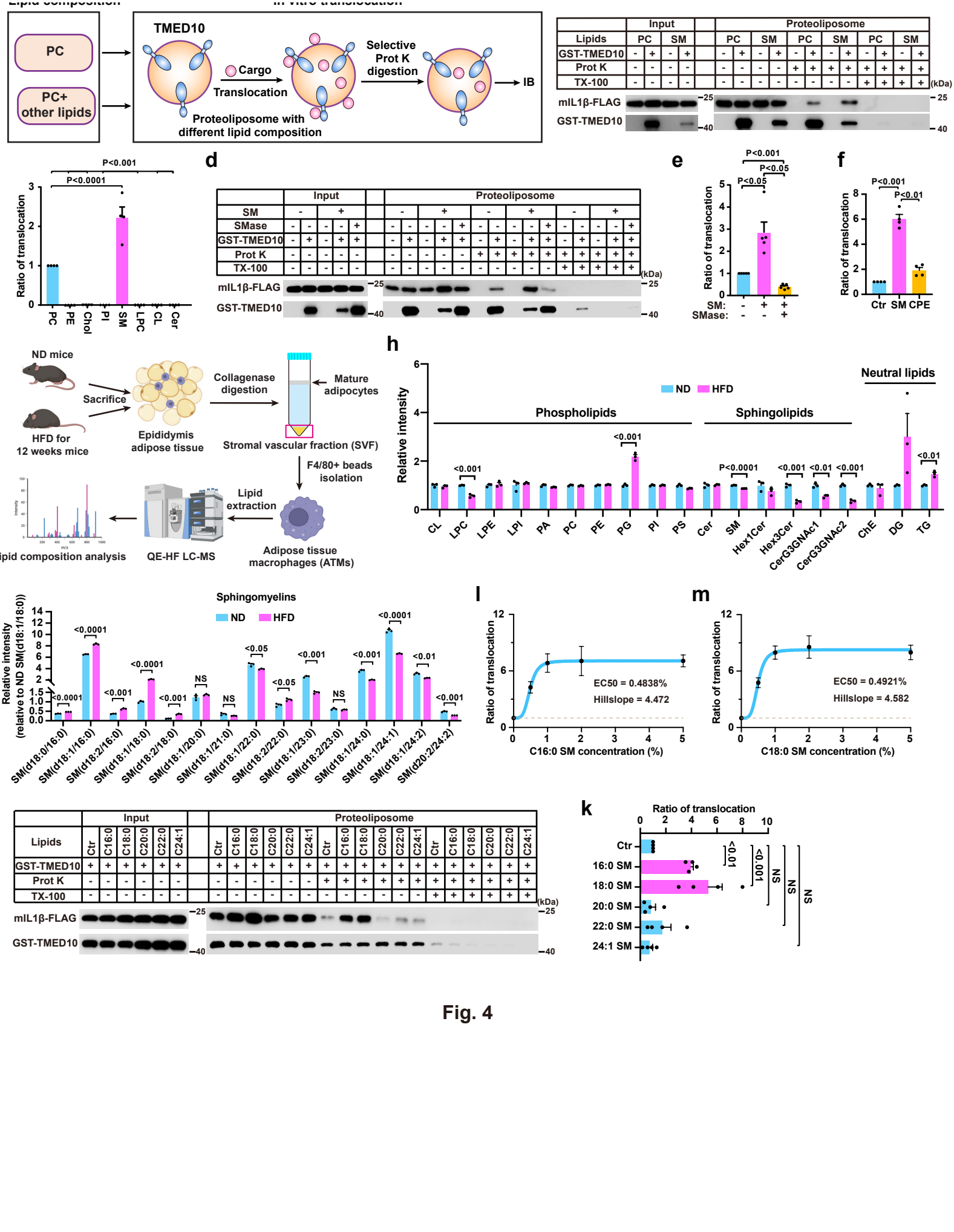

Fig. 4

Fig. 4 | TMED10 responds to medium chain SM. a, A schematic diagram showing the proteoliposomes with specific lipid composition were generated for the in vitro mIL-1β translocation assay. **b,** In vitro mIL-1β translocation assay using control or GST-TMED10 proteoliposomes of PC, or PC plus 10% SM. **c,** Quantification of the mIL-1β translocation efficiency (mean ± s.e.m.) in GST-TMED10 proteoliposomes of PC, or PC plus other lipids as shown in (**b**) and (**Extended Data Fig. 5b-e**). P values were calculated by one-way ANOVA (n = 4). Chol: cholesterol; LPC: lyso PC; CL: cardiolipin; Cer: ceramide. **d,** In vitro mIL-1β translocation assay using control or GST-TMED10 proteoliposomes of PC, PC plus SM, or PC plus SM treated with sphingomyelinase. **e,** Quantification of the mIL-1β translocation efficiency (mean ± s.e.m.) from (**d**). P values were calculated by one-way ANOVA (n = 5). **f,** Quantification of the mIL-1β translocation efficiency (mean ± s.e.m.) in GST-TMED10 proteoliposomes generated with PC (Ctr), PC plus 1% SM (C18:0) or 1% CPE (C18:0) as shown in (**Extended Data Fig. 5f**). P values were calculated by one-way ANOVA (n = 4). **g,** The workflow of ATMs separation and lipidomics analysis using ND and HFD mice. **h,** The relative intensity of different classes of lipids in ATMs from ND and HFD mice. The corresponding full name of these lipids are shown in **Supplementary Table 4**. **i,** The relative intensity of different subtypes of SM in ATMs from ND and HFD mice. **j,** In vitro mIL-1β translocation assay using GST-TMED10 proteoliposomes generated with PC (Ctr) or PC plus 1% SM with different length of acetyl fatty acid chains. **k,** Quantification of mIL-1β translocation efficiency (mean ± s.e.m.) from (**j**). P values were calculated by one-way ANOVA (n = 4). **l, m,** The dose response of TMED10-mediated mIL-1β translocation activated by C16:0 (**l**) or C18:0 (**m**) SM as shown in (**Extended Data Fig. 5g**) and (**Extended Data Fig. 5h**), respectively. Data are plotted as the mean ± s.e.m. from four independent experiments. The curve is typically fitted using the Four-parameter logistic equation with EC50 (the half-way response concentration) and Hill slope (a parameter describing the steepness of the curve) indicated.

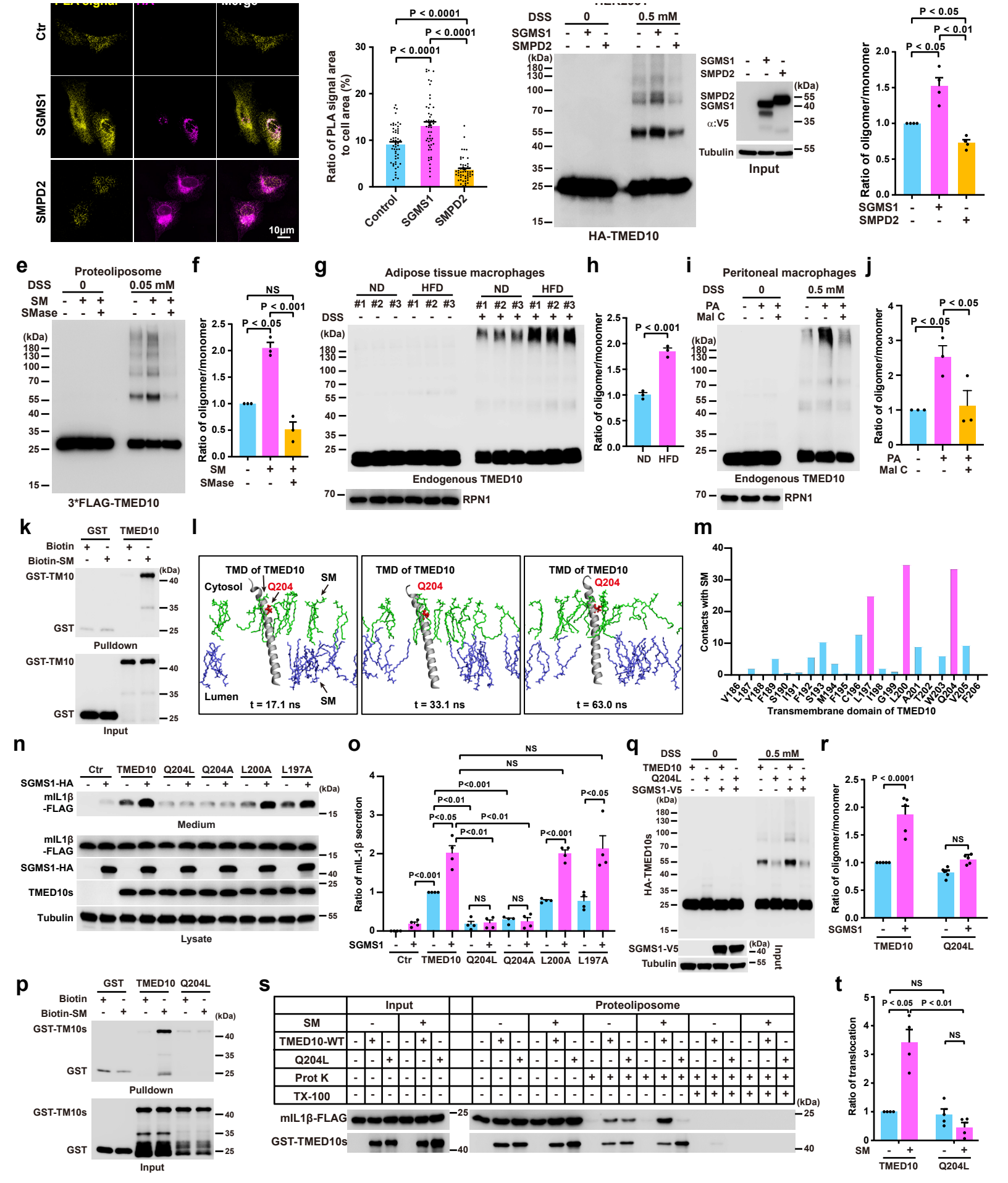

Fig. 5

Fig. 5 | SM binds and increases TMED10 oligomerization. a, Duolink PLA assay performed with U2OS cells co-expressing TMED10-V5, and TMED10-3*FLAG, without or with SGMS1-HA or SMPD2-HA to test the self-interaction of TMED10. Scale bar, 10 μm. **b,** Quantification of the percentage of duolink signal area to cell area (mean ± s.e.m.). P values were calculated by one-way ANOVA (> 50 cells from three independent experiments). **c,** Crosslink assay performed in HEK293T cells co-expressing HA-TMED10 without or with SGMS1-V5, or SMPD2-V5. **d,** Quantification of the ratio of TMED10 oligomers to its monomer from (**c**) (mean ± s.e.m.). P values were calculated by one-way ANOVA (n = 4). **e,** Crosslink assay performed in 3*FLAG-TMED10 proteoliposomes generated with PC, PC plus SM, or PC plus SM treated with sphingomyelinase. 3*FLAG-TMED10 was purified using the 293F expression system. **f,** Quantification of the ratio of TMED10 oligomers to its monomer from (**e**) (mean ± s.e.m.). P values were calculated by one-way ANOVA (n = 3). **g,** Crosslink assay using adipose tissue macrophages separated from ND and HFD mice. **h,** Quantification of the ratio of TMED10 oligomers to its monomer from (**g**) (mean ± s.e.m.). P value was calculated by two-tailed t test (n = 3). **i,** Crosslink assay using peritoneal macrophages treated without or with 200 μM PA or 200 μM PA plus 10 μM Malabaricone C (Mal C) for 16 h. **j,** Quantification of the ratio of TMED10 oligomers to its monomer from (**i**) (mean ± s.e.m.). P values were calculated by one-way ANOVA (n = 3). **k,** Pull-down assay performed between biotin-SM and GST or GST-TMED10. The data are representative of three independent experiments. **l,** Molecular dynamics simulations showing the interaction between the TMED10 transmembrane domain (TMD) and SM at three representative time points with Q204 highlighted. The corresponding video is shown in (**Supplementary Video 1**). **m,** Quantification of contact scores between TMED10 transmembrane domain residues and SM from (**l**). **n,** Secretion of mIL-1β in TMED10-KO HEK293T cells co-expressing control, TMED10-WT or mutants without or with SGMS1-HA. **o,** Quantification of mIL-1β secretion from (**n**) (mean ± s.e.m.). P values were calculated by one-way ANOVA (n = 4). **p,** Pull-down assay performed using biotin-SM and GST, GST-TMED10, or GST-TMED10-Q204L. The data are representative of three independent experiments. **q,** Crosslink assay performed in TMED10-KO HEK293T cells co-expressing HA-TMED10 or HA-TMED10-Q204L, without or with SGMS1-V5. **r,** Quantification of ratio of TMED10 oligomers to its monomer from (**q**) (mean ± s.e.m.). P values were calculated by one-way ANOVA (n = 5). **s,** In vitro mIL-1β translocation assay using control，GST-TMED10 or GST-TMED10-Q204L proteoliposomes generated with PC, or PC plus 10% SM respectively. **t,** Quantification of the relative translocation efficiency of mIL-1β from (**s**) (mean ± s.e.m.). P values were calculated by one-way ANOVA (n = 4).

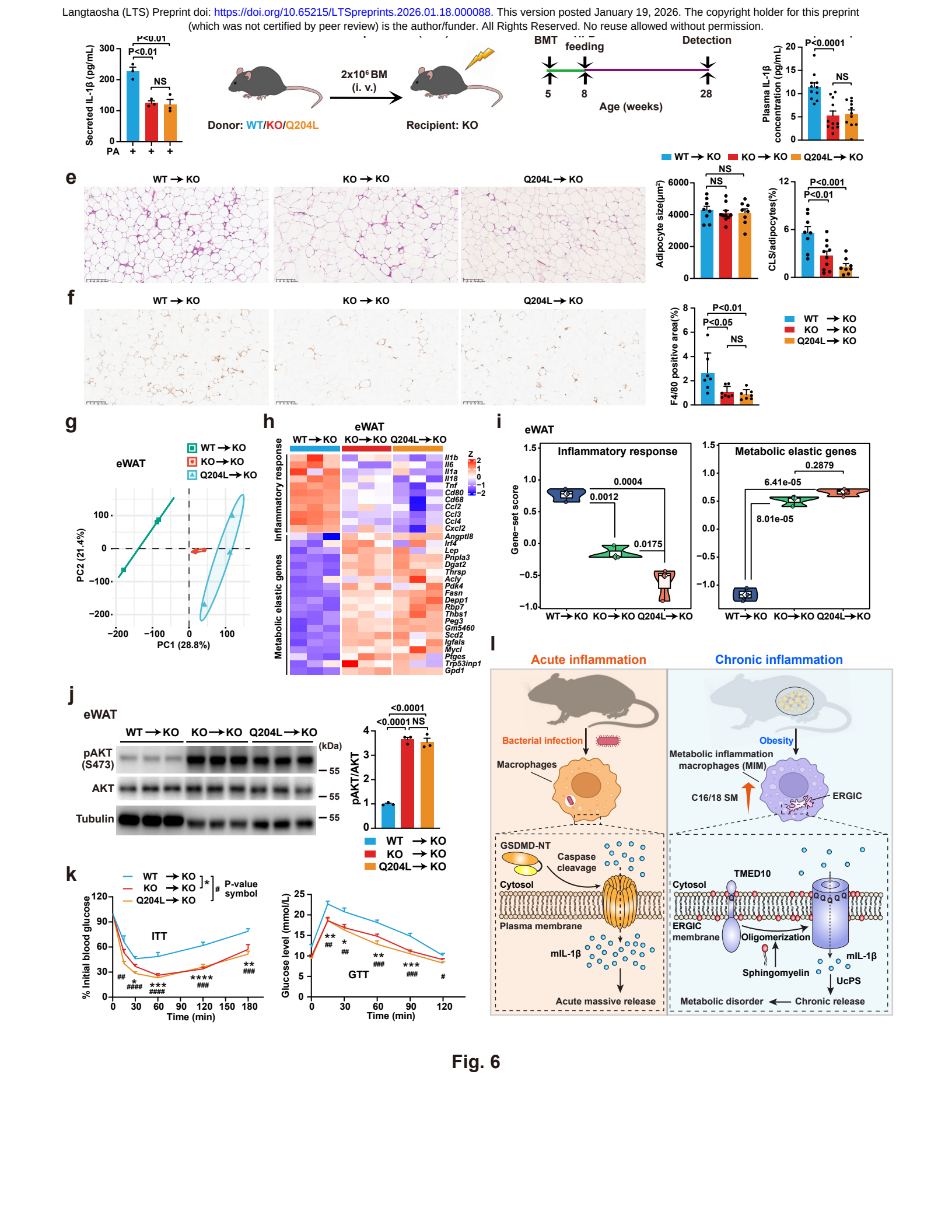

Fig. 6

Fig. 6 | TMED10-Q204L mutant alleviates HFD-induced metabolic inflammation and dysfunction. a, ELISA analysis of IL-1β secretion in peritoneal macrophages following 150 μM PA stimulation for 24 h from WT (*TMED10*$^{fl/fl}$), KO (*Lyz2*-cre *TMED10*$^{fl/fl}$) or TMED10-Q204L knock-in (*TMED10*$^{Q204L/Q204L}$) mice. **b,c,** Scheme of bone marrow transplantation (BMT) assay. **d**, ELISA analysis of plasma IL-1β (n=11) from KO (*Lyz2*-cre *TMED10*$^{fl/fl}$) mice transplanted with bone marrows of WT (*TMED10*$^{fl/fl}$), KO (*Lyz2*-cre *TMED10*$^{fl/fl}$) or Q204L knock-in (*TMED10*$^{Q204L/Q204L}$) mice after HFD. **e**, H&E staining of eWAT for quantification of adipocyte size and CLS percentage (n=8-10). **f**, IHC for F4/80+ macrophages in eWAT (n=7). **g**, PCA of eWAT from RNA-seq. **h,i,** Heatmap analysis (**h**) of genes involved in inflammatory response or metabolic elastic genes with corresponding gene-set score (**i**) in eWAT. **j**, Western blot analysis of pAKT (S473) and quantification in eWAT after insulin administration for 15 min (n=3). **k**, GTT (n=6) and ITT (n=6-8) of indicated BMT mice fed with HFD. NS, non-significant; */$^{\#}$ $P < 0.05$; **/$^{\#\#}$ $P < 0.01$; ***/$^{\#\#\#}$ $P < 0.001$; ****/$^{\#\#\#\#}$ $P < 0.0001$. All values are presented as mean ± s.e.m. P values were calculated by one-way ANOVA followed by Tukey's test (**a, d, e, f, j, k**), or two-sided Wilcoxon rank-sum test (**i**). **l**, A model comparing GSDMD-mediated acute inflammation with TMED10-mediated chronic metabolic inflammation. During bacterial infection, acute inflammation is driven by the rapid release of IL-1β from macrophages, a process triggered by gasdermin-D–mediated pore formation. In contrast, metabolic inflammation is characterized by a chronic, low-grade inflammatory response in which macrophages accumulate lipids, resulting in altered sphingomyelin composition. Specifically, an increase in medium-chain SM species promotes TMED10 oligomerization and activation—likely occurring at the ERGIC—which in turn enables a slow, sustained release of IL-1β. This mechanism underlies the persistent inflammatory tone associated with metabolic disease.

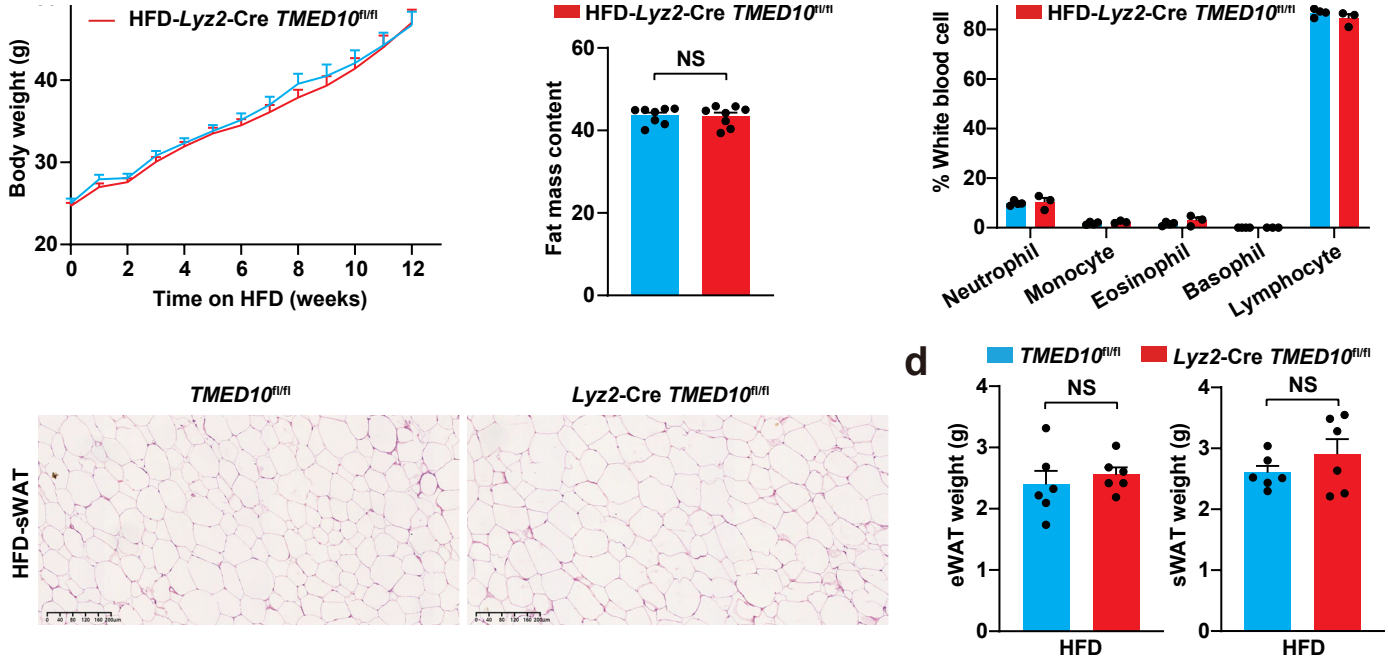

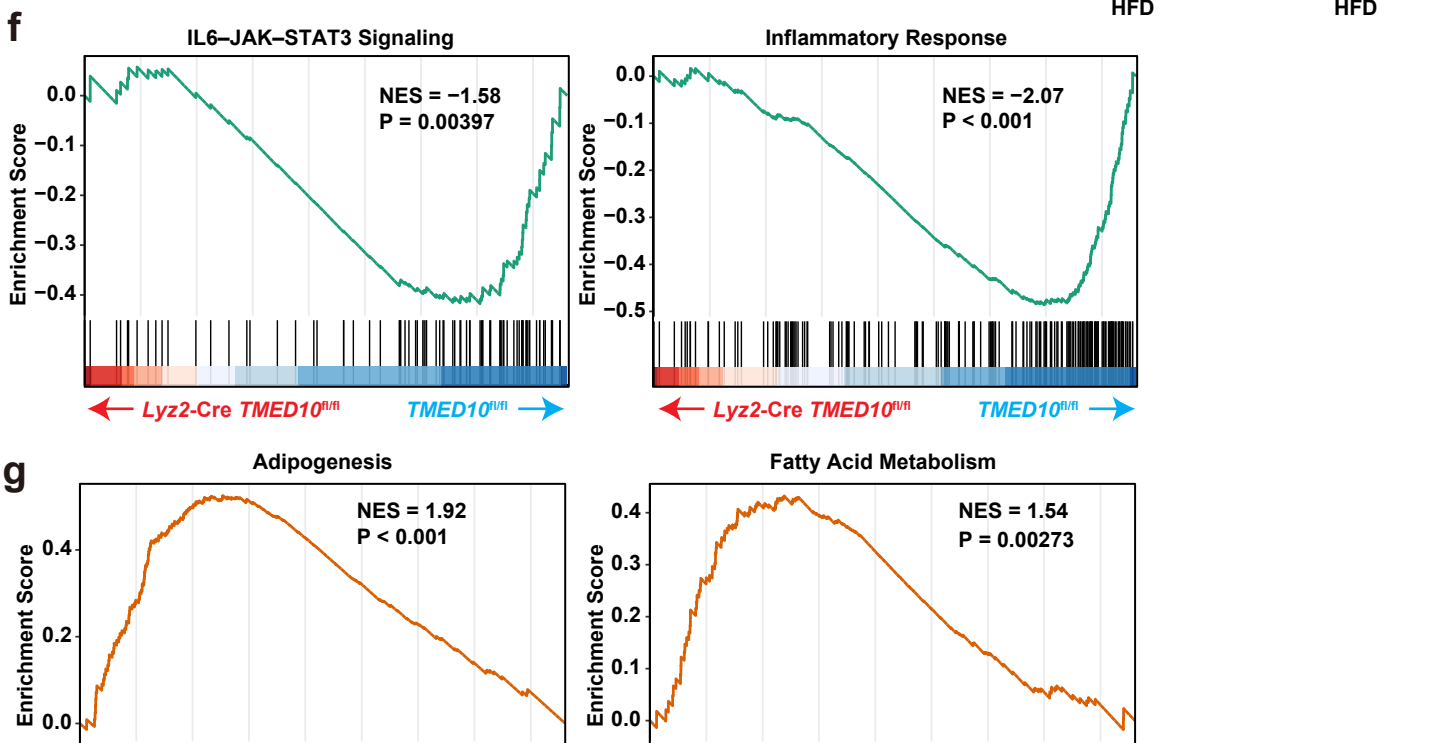

Extended Data Fig. 1

Extended Data Fig. 1 | Myeloid TMED10 deficiency mitigates HFD-induced metabolic inflammation and metabolic dysfunction independent of body or WAT weights. Male *TMED10*$^{fl/fl}$ mice and *Lyz2*-cre *TMED10*$^{fl/fl}$ mice were fed on HFD for 12 weeks. The following analyses were performed, including: **a**, Body weights (n=6); **b**, Fat mass content (n=8); **c**, H&E staining of sWAT; **d**, eWAT and sWAT weights(n=6); **e**, Percentage of white blood cells (n=3); **f, g,** GSEA analysis of indicated biological processes from bulk RNA-seq of eWAT shown in (**Fig. 1m-q**). All values are presented as mean ± s.e.m. P values were calculated by unpaired two-tailed Student's t-test (**b, d**) or permutation testing adjusted for multiple comparisons using the Benjamini–Hochberg procedure (**f, g**).

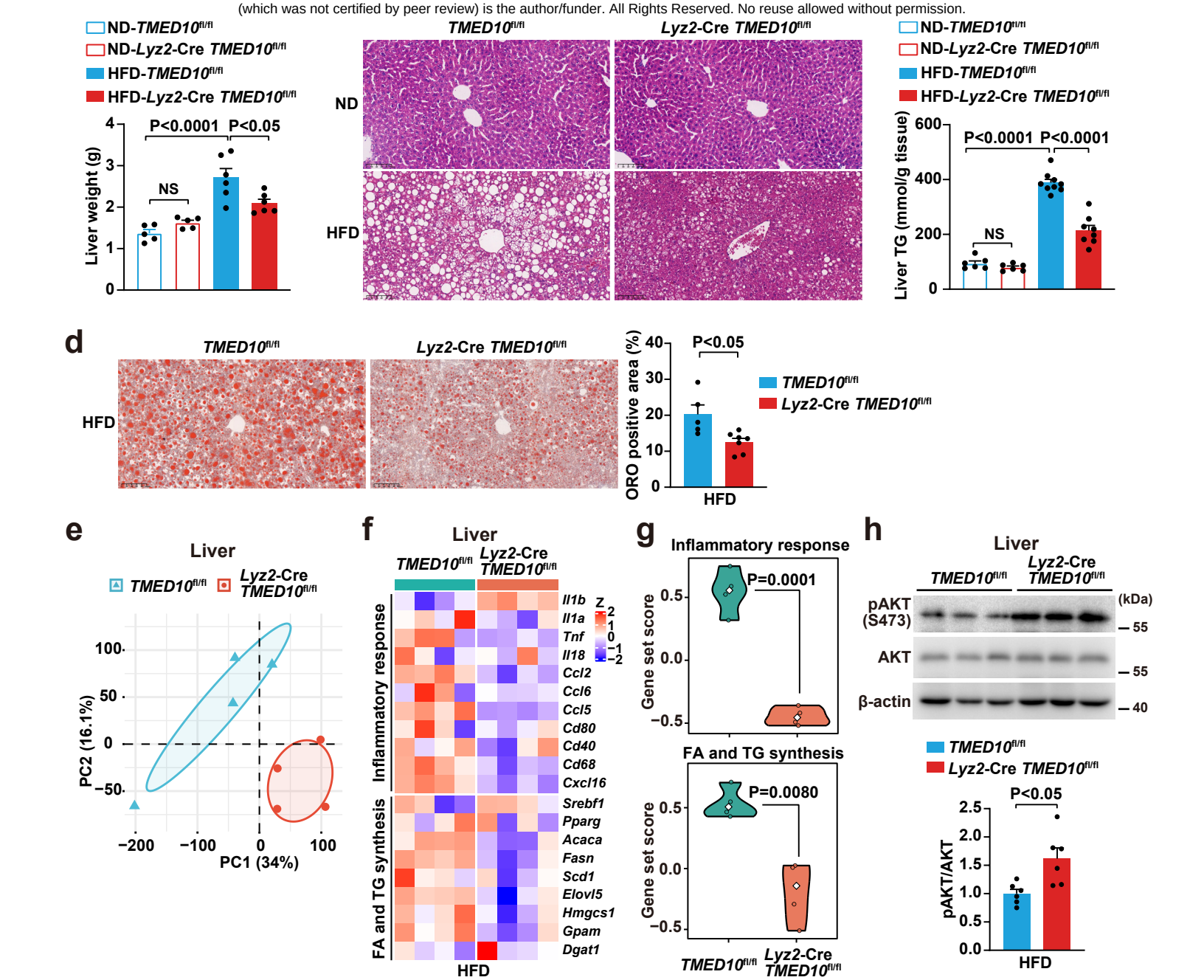

Extended Data Fig. 2

Extended Data Fig. 2 | Myeloid TMED10 deficiency alleviates HFD-induced hepatic lipid accumulation and metabolic function. Male *TMED10*$^{fl/fl}$ mice and *Lyz2*-cre *TMED10*$^{fl/fl}$ mice were fed on ND or HFD for 12 weeks. The following analyses were performed, including: **a**, Liver weight (n=5-6). **b**, H&E staining of liver. **c**, Liver TG (n=6-9). **d**, Oil Red O staining of liver (n=5-7). **e**, PCA of liver from RNA-seq. **f, g**, Heatmap analysis (**f**) of genes involved in inflammatory response or metabolic elastic genes with corresponding gene-set score (**g**) in liver. **h**, Western blot analysis of pAKT (S473) and quantification in liver after insulin administration for 15 min (n=6). All values are presented as mean ± s.e.m. P values were calculated by unpaired two-tailed Student's t-test (**d, h**), two-sided Wilcoxon rank-sum test (**g**), or one-way ANOVA followed by Tukey's test (**a, c**).

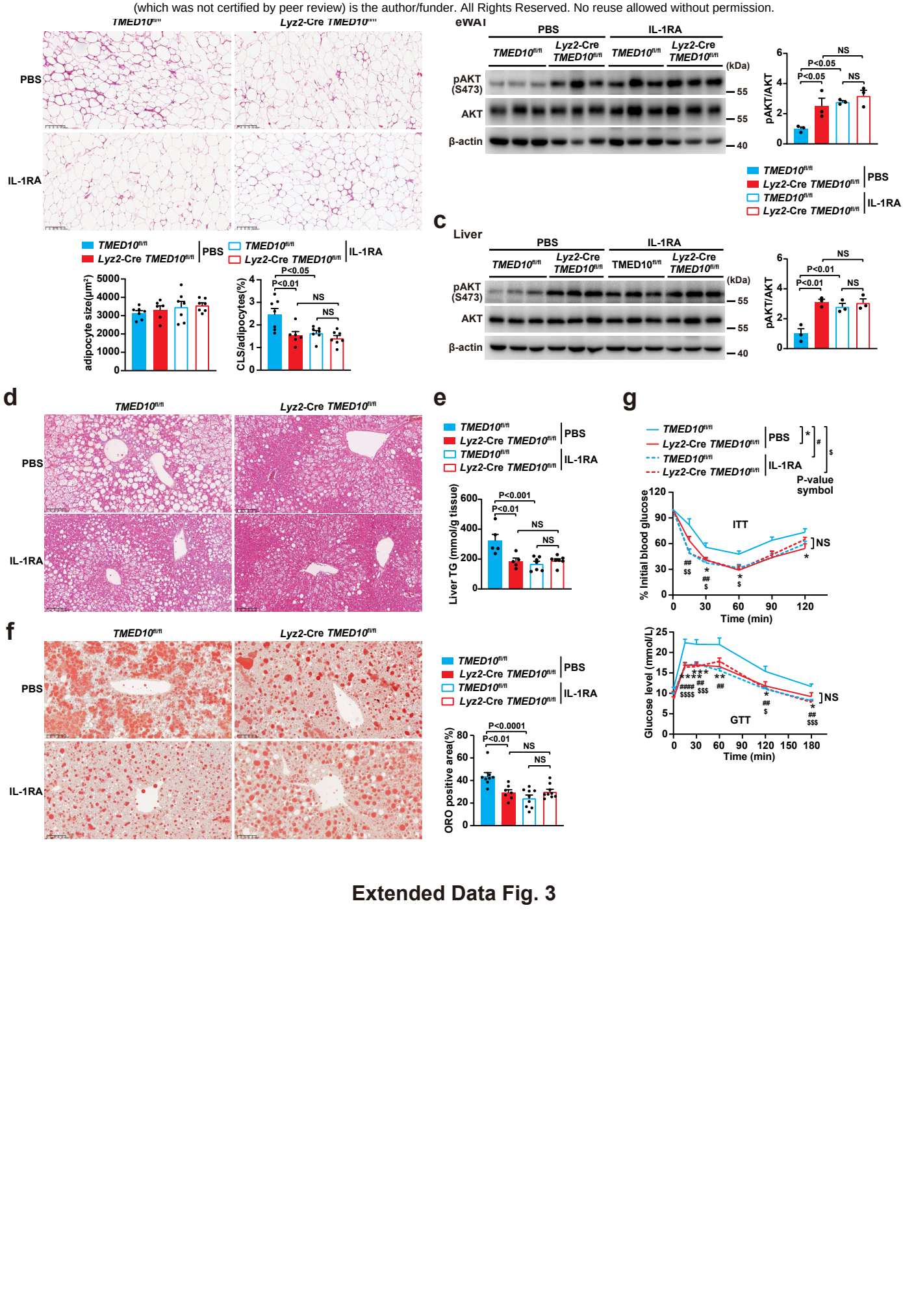

Extended Data Fig. 3

Extended Data Fig. 3 | IL-1β is the major pro-inflammatory cytokine accounting for the effect of TMED10 deficiency. Male *TMED10*$^{fl/fl}$ mice and *Lyz2*-cre *TMED10*$^{fl/fl}$ mice were fed on HFD for 4 weeks, then mice were intraperitoneally injected with 10 mg/kg IL-1RA or PBS every other day for 8 weeks. The following analyses were performed, including: **a**, H&E staining of eWAT for quantification of adipocyte size and crown-like structure (CLS) percentage (n=6-7). **b, c**, Western blot analysis of pAKT (S473) and quantification in eWAT (**b**) and liver (**c**) after insulin administration for 15 min (n=3). **d**, H&E staining of liver. **e**, Liver TG (n=5-7). **f**, Oil Red O staining of liver (n=7-9). **g,** GTT (n=9) and ITT (n=7)**.** NS, non-significant; */#/$ P < 0.05; **/##/$$ P < 0.01; ***/###/$$$ P < 0.001; ****/####/$$$$ P < 0.0001. All values are presented as mean ± s.e.m. P values were calculated by one-way ANOVA followed by Tukey's test (**a-c**, **e-g**).

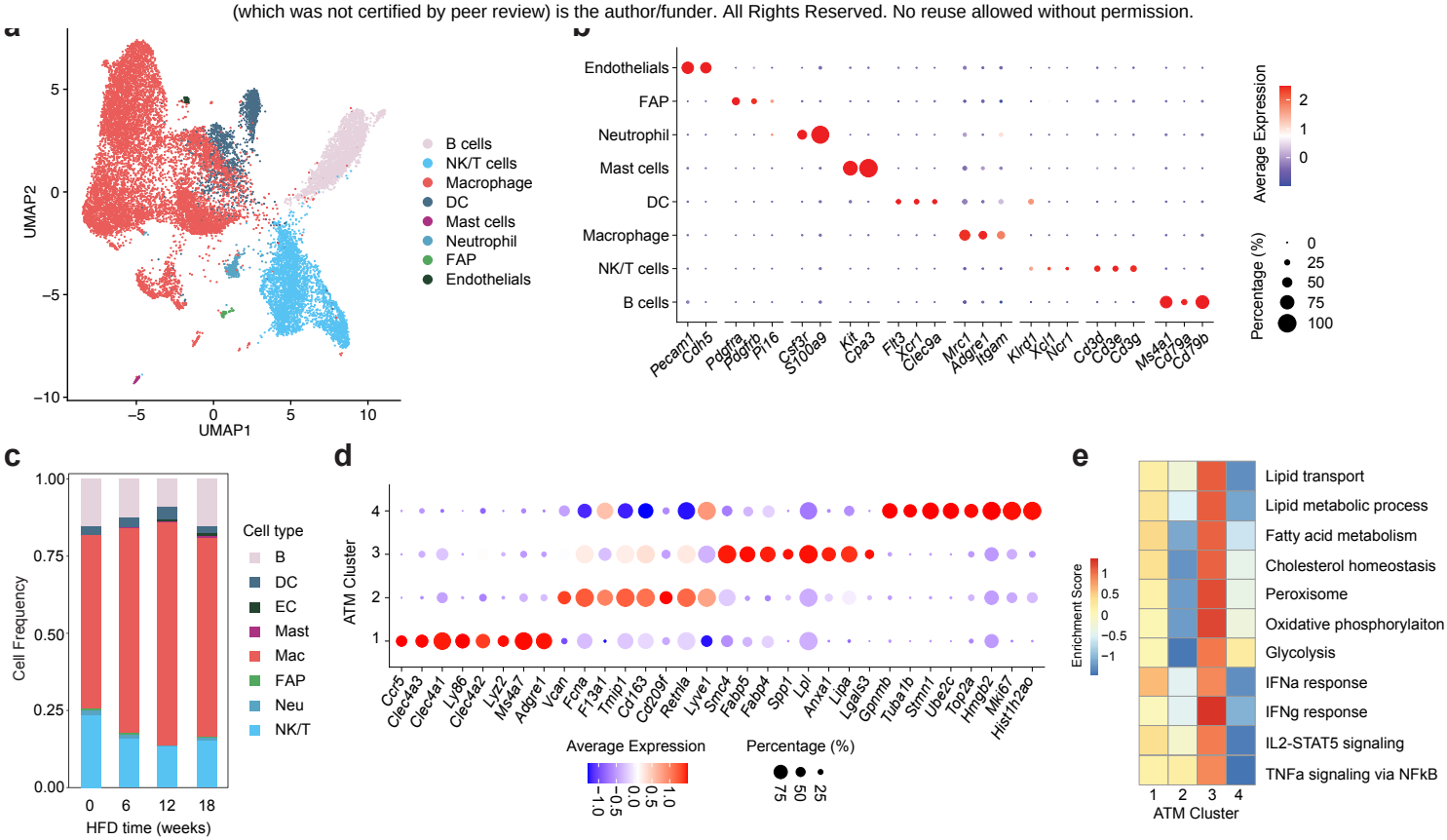

Extended Data Fig. 4

Extended Data Fig. 4 | Single-cell definition of adipose stromal cell populations and conserved ATM subsets in mouse and human adipose tissue. a, UMAP visualization of stromal vascular cells from mouse eWAT colored by major cell types (B cells, NK/T cells, macrophages, dendritic cells (DCs), mast cells, neutrophils, fibro-adipogenic progenitors (FAP), and endothelial cells) identified by canonical markers. **b,** Dot plot of representative marker genes for each stromal cell type shown in (**a**); dot size indicates the percentage of cells expressing the gene, and color denotes scaled average expression. **c,** Bar graph showing the relative frequency of each stromal cell type in eWAT across increasing durations of HFD feeding (0, 6, 12, and 18 weeks). **d,** Dot plot of marker genes defining four transcriptionally distinct ATM clusters (1–4) in mouse eWAT shown in (**Fig. 2c-g**). Dot size indicates the percentage of cells expressing the gene, and color denotes scaled average expression. **e,** Heatmap of enrichment scores for lipid metabolic and inflammatory pathways (lipid transport, fatty acid metabolism, cholesterol homeostasis, peroxisome, oxidative phosphorylation, glycolysis, IFNα/IFNγ responses, IL-2–STAT5 signaling, and TNFα–NFκB signaling) in mouse ATM clusters 1–4. **f,** UMAP visualization of myeloid populations from human adipose tissue, showing neutrophils, macrophages, monocytes, and three DC subsets (DC_1–3). **g,** Dot plot of representative marker genes for human neutrophil, macrophage, monocyte, and DC subsets shown in (**f**); dot size indicates the percentage of cells expressing the gene, and color denotes scaled average expression. **h,** Dot plot of representative marker genes for human ATMs clusters (1–4) shown in (**Fig. 2i-m**); dot size indicates the percentage of cells expressing the gene, and color denotes scaled average expression. **i,** Heatmap of enrichment scores for lipid metabolic and inflammatory pathways (lipid transport, fatty acid metabolism, cholesterol homeostasis, peroxisome, oxidative phosphorylation, glycolysis, IFNα/IFNγ responses, IL-2–STAT5 signaling, and TNFα–NFκB signaling) in human ATM clusters 1–4.

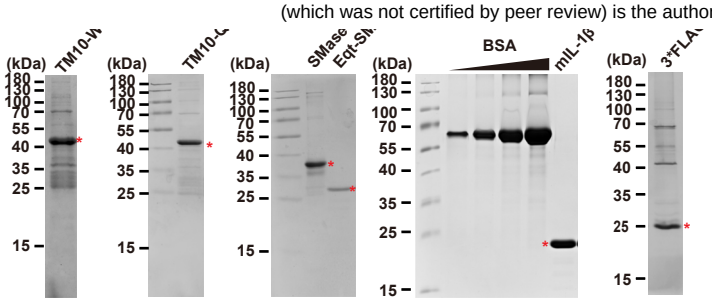

b

Lipids	Input PI	Input SM	Proteoliposome PI				Proteoliposome SM			
GST-TMED10	- +	- +	- +	- +	- +	- +	- +	- +	- +	- +
Prot K	- -	- -	- -	+ +	+ +	+ +	- -	+ +	+ +	+ +
TX-100	- -	- -	- -	- -	+ +	+ +	- -	- -	- +	+ +

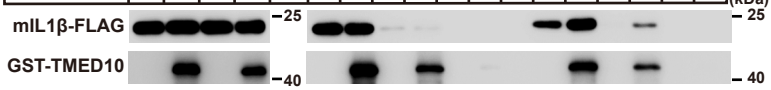

c

Lipids	Input PE	Input Chol	Proteoliposome PE	Chol	PE	Chol	PE	Chol
GST-TMED10	- +	- +	- +	- +	- +	- +	- +	- +
Prot K	- -	- -	- -	- -	+ +	+ +	+ +	+ +
TX-100	- -	- -	- -	- -	- -	- -	+ +	+ +

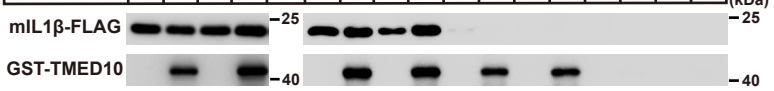

d

Lipids	Input LPC	Input CL	Proteoliposome LPC	CL	LPC	CL	LPC	CL
GST-TMED10	- +	- +	- +	- +	- +	- +	- +	- +
Prot K	- -	- -	- -	- -	+ +	+ +	+ +	+ +
TX-100	- -	- -	- -	- -	- -	- -	+ +	+ +

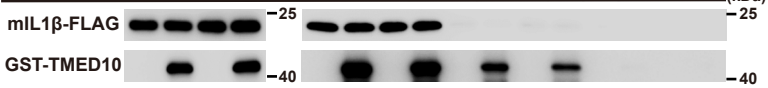

e

Lipids	Input PC	Input Cer	Proteoliposome PC	Cer	PC	Cer	PC	Cer
GST-TMED10	- +	- +	- +	- +	- +	- +	- +	- +
Prot K	- -	- -	- -	- -	+ +	+ +	+ +	+ +
TX-100	- -	- -	- -	- -	- -	- -	+ +	+ +

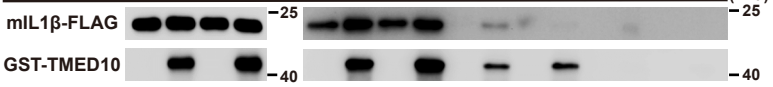

f

Lipids	Input Ctr	Input SM	Input CPE	Input Ctr	Input SM	Input CPE	Proteoliposome Ctr	SM	CPE	Ctr	SM	CPE	Ctr	SM	CPE	Ctr	SM	CPE	Ctr	SM	CPE	Ctr	SM	CPE
GST-TMED10	-	-	-	+	+	+	-	-	-	+	+	+	-	-	-	+	+	+	-	-	-	+	+	+
Prot K	-	-	-	-	-	-	-	-	-	-	-	-	+	+	+	+	+	+	+	+	+	+	+	+
TX-100	-	-	-	-	-	-	-	-	-	-	-	-	-	-	-	-	-	-	+	+	+	+	+	+

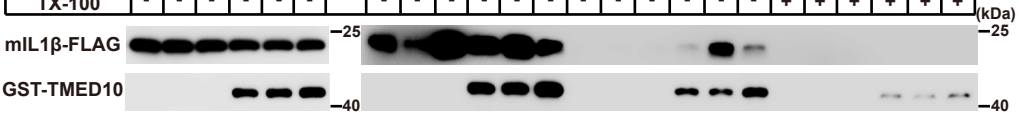

g

C16:0 SM (%)	Input 0	0.5	1	2	5	10	Proteoliposome 0	0.5	1	2	5	10	0	0.5	1	2	5	10	0	0.5	1	2	5	10
GST-TMED10	+	+	+	+	+	+	+	+	+	+	+	+	+	+	+	+	+	+	+	+	+	+	+	+	+
Prot K	-	-	-	-	-	-	-	-	-	-	-	-	+	+	+	+	+	+	+	+	+	+	+	+	+
TX-100	-	-	-	-	-	-	-	-	-	-	-	-	-	-	-	-	-	-	+	+	+	+	+	+	+

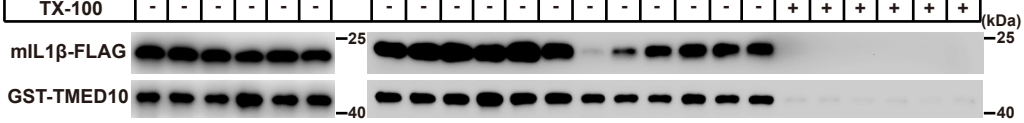

h

C18:0 SM (%)	Input 0	0.5	1	2	5	Proteoliposome 0	0.5	1	2	5	0	0.5	1	2	5	0	0.5	1	2	5
GST-TMED10	+	+	+	+	+	+	+	+	+	+	+	+	+	+	+	+	+	+	+	+	+
Prot K	-	-	-	-	-	-	-	-	-	-	+	+	+	+	+	+	+	+	+	+	+
TX-100	-	-	-	-	-	-	-	-	-	-	-	-	-	-	-	+	+	+	+	+	+

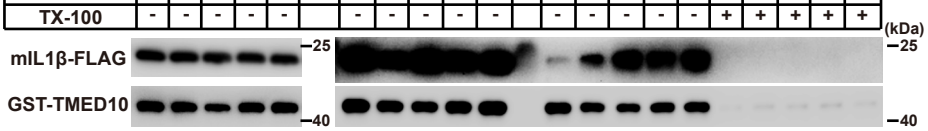

Extended Data Fig. 5

Extended Data Fig. 5 | Protein purification and effect of lipids for TMED10-mediated IL-1β translocation. a, Coomassie blue staining of GST-TMED10, GST-TMED10-Q204L, Sphingomyelinase (SMase), Equinatoxin II (Eqt-SM) and T7-mIL-1β-FLAG purified from *E. coli* expression system; and 3*FLAG-TMED10 purified using the 293F mammalian expression system. **b-e,** In vitro mIL-1β translocation assay using control or GST-TMED10 proteoliposomes generated with PC, or PC plus 10% other lipids (PI, SM, PE, Cholesterol, lyso PC, cardiolipin and ceramide). Chol: cholesterol; LPC: lyso PC; CL: cardiolipin; Cer: ceramide. **f,** In vitro mIL-1β translocation assay using control or GST-TMED10 proteoliposomes generated with PC (Ctr), PC plus 1% SM (C18:0) or 1% CPE (C18:0). **g, h,** In vitro mIL-1β translocation assay using GST-TMED10 proteoliposomes generated with PC, or PC plus indicated concentration of C16:0 (**g**) or C18:0 (**h**) SM.

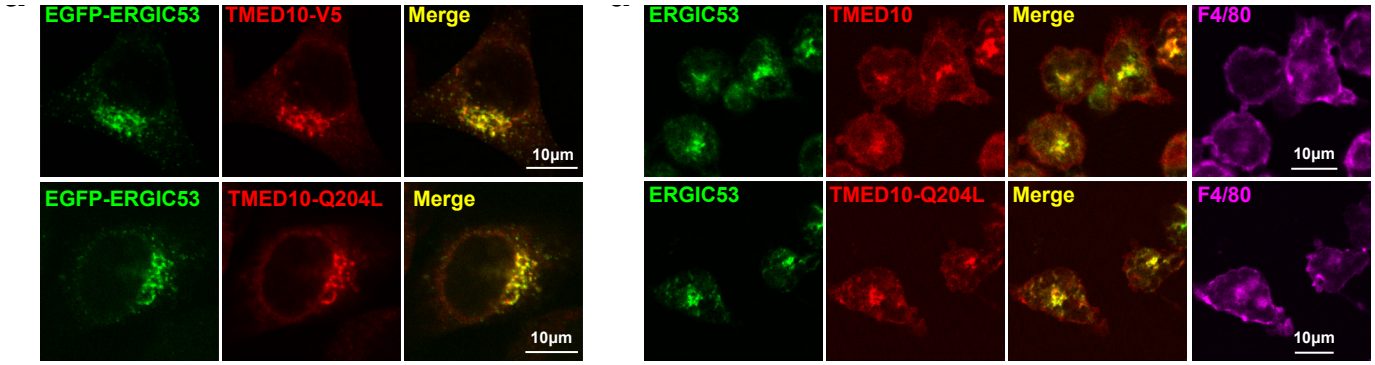

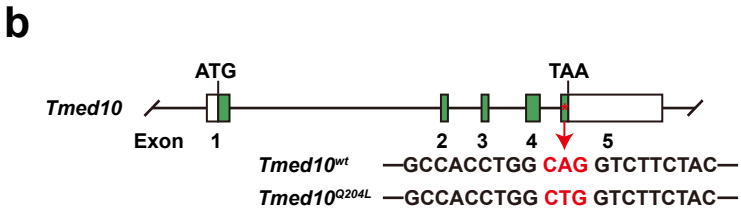

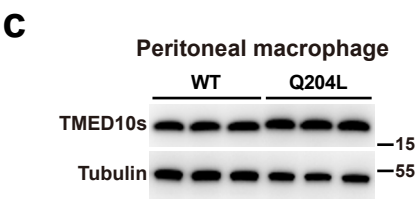

Extended Data Fig. 6

Extended Data Fig. 6 | Localization and expression of TMED10-Q204L mutant. a, Immunofluorescence of TMED10 KO HeLa cells co-expressing EGFP-ERGIC-53 with TMED10-WT or Q204L mutant using anti-V5 antibodies. Scale bar, 10 μm. **b,** Scheme of TMED10-Q204L knock-in mice generation. **c, d,** The protein level (**c**) and localization (**d**) of endogenous TMED10 and Q204L mutant in peritoneal macrophages separated from WT and TMED10-Q204L knock-in mice.

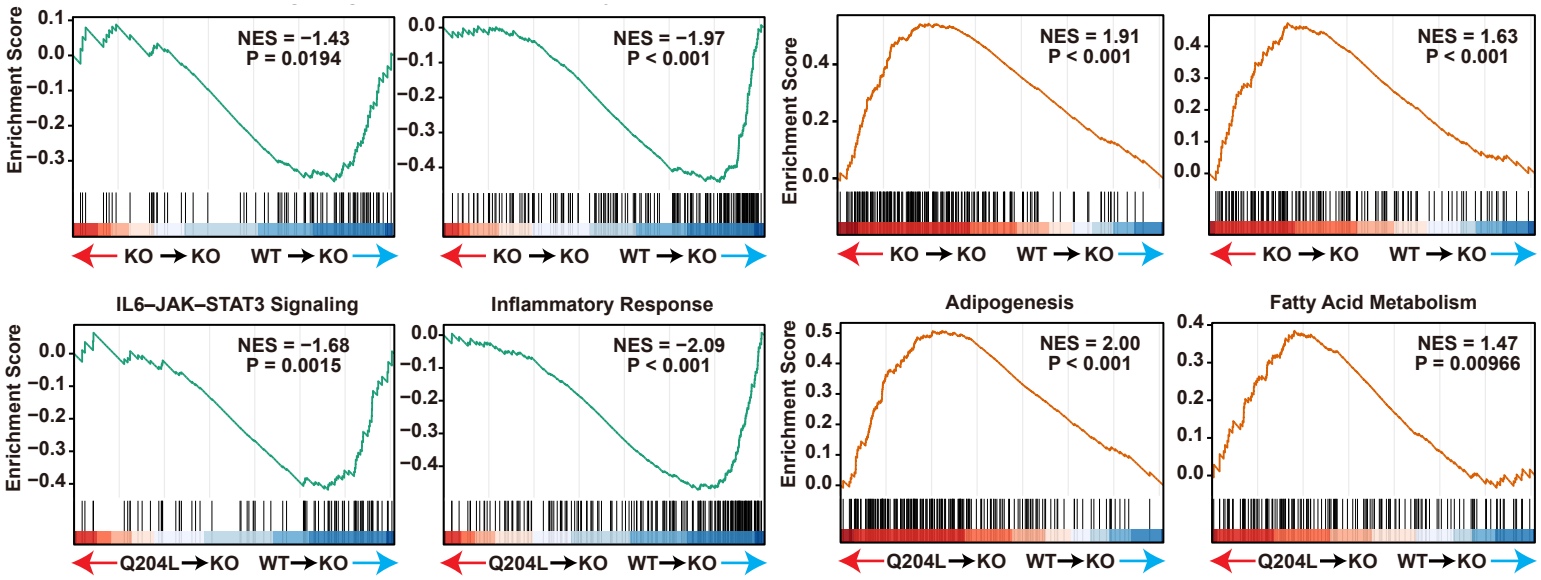

c

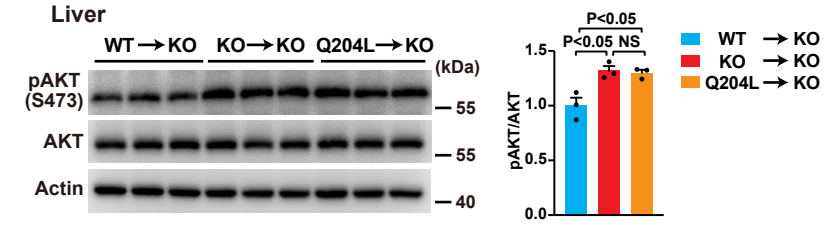

d

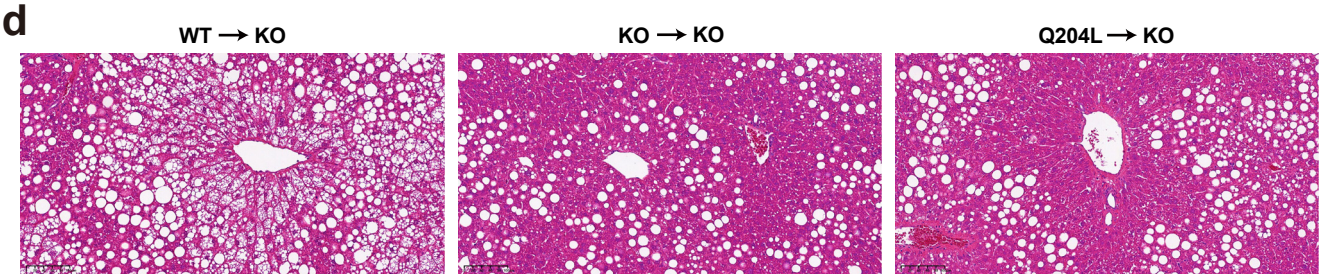

e

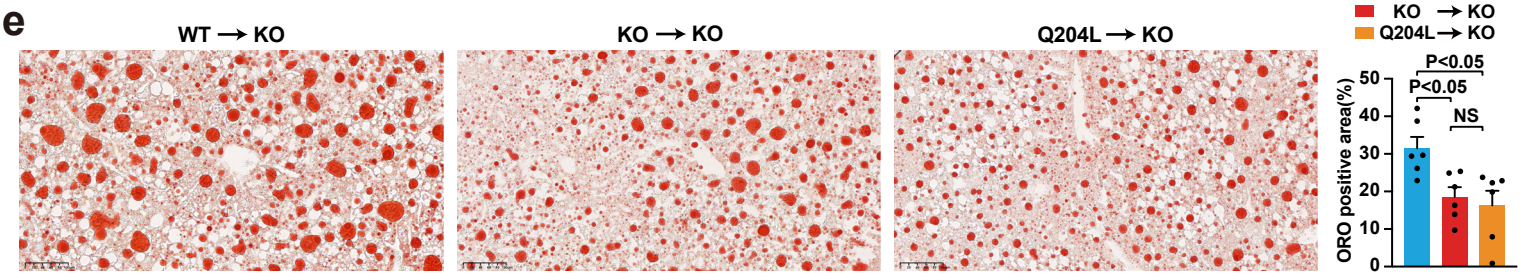

Extended Data Fig. 7

Extended Data Fig. 7 | TMED10-Q204L mutant alleviates HFD-induced adipose tissue inflammation and metabolic dysfunction, and hepatic metabolic dysfunction. a, b, GSEA analysis of indicated pathways from bulk RNA-seq of eWAT from bone marrow transplantation mice as shown in (**Fig. 6g-i**). **c**, Western blot analysis of pAKT (S473) and quantification in liver after insulin administration for 15 min (n=3). **d**, H&E staining of liver. **e**, Oil Red O staining of liver (n=6). All values are presented as mean ± s.e.m. P values were calculated by permutation testing adjusted for multiple comparisons using the Benjamini–Hochberg procedure (**a, b**), or one-way ANOVA followed by Tukey's test (**c, e**).